CONTROL OF FLOW STRUCTURE ON 45 DEGREE SWEPT DELTA WING
USING PASSIVE BLEEDING

A THESIS SUBMITTED TO
THE GRADUATE SCHOOL OF NATURAL AND APPLIED SCIENCES
OF
MIDDLE EAST TECHNICAL UNIVERSITY

BY

BURCU KARAGÖZ

IN PARTIAL FULFILLMENT OF THE REQUIREMENTS
FOR
THE DEGREE OF MASTER OF SCIENCE
IN
MECHANICAL ENGINEERING

SEPTEMBER 2017

Approval of the thesis:

CONTROL OF FLOW STRUCTURE ON 45 DEGREE SWEPT DELTA WING USING PASSIVE BLEEDING

submitted by **BURCU KARAGÖZ** in partial fulfillment of the requirements for the degree of **Master of Science in Mechanical Engineering Department, Middle East Technical University** by,

Prof. Dr. Gülbin Dural Ünver   _____
Dean, Graduate School of **Natural and Applied Sciences**

Prof. Dr. R. Tuna Balkan   _____
Head of Department, **Mechanical Engineering**

Assoc. Prof. Dr. Mehmet Metin Yavuz   _____
Supervisor, **Mechanical Engineering Dept., METU**

Examining Committee Members:

Assoc. Prof. Dr. Cüneyt Sert   _____
Mechanical Engineering Dept., METU

Assoc. Prof. Dr. M. Metin Yavuz   _____
Mechanical Engineering Dept., METU

Assist. Prof. Dr. Feyza Kazanç   _____
Mechanical Engineering Dept., METU

Assoc. Prof. Dr. Dilek Funda Kurtuluş   _____
Aerospace Engineering Dept., METU

Assoc. Prof. Dr. Murat Kadri Aktaş   _____
Mechanical Engineering Dept., TOBB University

Date: 07.09.2017

I hereby declare that all information in this document has been obtained and presented in accordance with academic rules and ethical conduct. I also declare that, as required by these rules and conduct, I have fully cited and referenced all material and results that are not original to this work.

Name, Last name: Burcu KARAGÖZ

Signature :

ABSTRACT

CONTROL OF FLOW STRUCTURE ON 45 DEGREE SWEPT DELTA WING
USING PASSIVE BLEEDING

Karagöz, Burcu

M.Sc., Department of Mechanical Engineering

Supervisor : Assoc. Prof. Dr. Mehmet Metin Yavuz

September 2017, 78 pages

In recent decades, researchers aim to understand and control the physical
phenomenon behind the complex flow structure of low swept delta wings arising
with their widespread use in Unmanned Air Vehicles (UAV), Unmanned Combat
Air Vehicles (UCAV) and Micro Air Vehicles (MAV). In order to extend the
working capabilities of these vehicles with having stable flight performance,
detailed studies on understanding and controlling the flow structures over low
swept delta wings are required.

The aim of the present study is to control the flow structure over a non-slender
delta wing with sweep angle of $\Lambda = 45$ degree using passive bleeding with
particular interest in eradication of three-dimensional surface separation. The
passive bleeding is a method, which uses simple passages inside the wing and
allows the fluid flow from the pressure side to the suction side using the inherent
pressure difference. The experiments are conducted in a low speed wind tunnel
using surface pressure measurements and Particle Image Velocimetry (PIV),
where the streamlines and the corresponding patterns of velocity and vorticity are

characterized on a plane immediately adjacent to the surface of the wing. Three different bleeding configurations with back angles $\beta = 13, 18$ and 23 degrees, where these angles define the bleeding passage orientations with respect to free stream velocity, are tested to quantify the effect of passive bleeding with back angle on flow structure compared to Base planform for broad ranges of Reynolds numbers $3.5 \times 10^4 < Re < 12.5 \times 10^4$ and attack angles $13 \leq \alpha \leq 23$ degrees. The results indicate that bleeding significantly alters the overall flow structure as shown in the near surface velocity, vorticity, and streamline patterns and the suction pressure coefficient $-C_p$. At sufficiently high angle of attack where the pronounced surface separation appears on the Base planform, which is indicated by focus point along with large-scale swirl in the near surface streamline pattern, the elimination of surface separation is achieved with passive bleeding. This is incorporated with significant increases in the magnitudes of surface normal vorticity and suction pressure coefficient $-C_p$, which indicate recovery of leading edge vortex. Considering the effect of back angle, β, on flow structure, $\beta = 23$ degree provides the utmost improvement on the overall flow pattern in terms of the elimination of three dimensional surface separation, where for certain angle of attack, $\beta = 18$ degree induces flow pattern which is quite similar to the one obtained by $\beta = 23$ degree.

Keywords: Non-slender delta wing, Low sweep angle, Leading edge vortex, Three-dimensional surface separation, Passive flow control, Bleeding.

ÖZ

45 DERECE OK AÇILI DELTA KANATLARIN PASİF AKITMA YÖNTEMİ İLE KONTROLÜ

Karagöz, Burcu

Yüksek Lisans, Makina Mühendisliği Bölümü

Tez Yöneticisi : Doç. Dr. Mehmet Metin Yavuz

Eylül 2017, 78 sayfa

Son yıllarda, araştırmacılar, İnsansız Hava Araçları (UAV), İnsansız Muharebe Hava Araçları (UCAV) ve Mikro Hava Araçlarında (MAV) yaygın kullanımları ile ortaya çıkan, düşük süpürme açılı delta kanatların karmaşık akış yapısının ardındaki fiziksel fenomeni anlamayı ve kontrol etmeyi amaçlamaktadırlar. Bu araçların uçuş performanslarını istikrarlı hale getirmek ve çalışma kabiliyetlerini geliştirmek için, düşük süpürme açılı delta kanatların üzerindeki akış yapılarını anlama ve kontrol etme konusunda ayrıntılı çalışmalara ihtiyaç vardır.

Bu çalışmanın amacı, pasif akıtma metodunu kullanarak, $\Lambda = 45$ derecelik süpürme açısına sahip bir delta kanadın üzerindeki akış yapısını, üç boyutlu yüzey ayrımının ortadan kaldırılmasını amaçlayarak kontrol etmektir. Pasif akıtma; kanadın içindeki basit geçitler sayesinde iç basınç farkını kullanarak havanın basınç tarafından emme tarafına akışını sağlayan bir yöntemdir. Deneyler, yüzey basınç ölçümleri ve parçacık görüntülemeli hız ölçüm tekniği (PIV) kullanılarak düşük hızlı bir rüzgar tünelinde gerçekleştirilmiştir. Serbest akış yönüne göre belirlenmiş, $\beta = 13, 18$ and 23 derece arka açılı üç kanat üzerinde, arka açı

konfigürasyonlu pasif akıtmanın akış yapısı üzerindeki etkisini Temel kanat yüzeyindeki akış yapısıyla kıyaslamak için, geniş bir hücum açısı aralığında $13 \leq \alpha \leq 23$ derece ve çeşitli Reynolds sayıları $3.5 \times 10^4 < Re < 12.5 \times 10^4$ için deneyler yapılmıştır. Yakın yüzey hızı, girdaplılık ve emme basınç katsayısı $-C_p$ sonuçlarında görüldüğü gibi, akıtma, kanat üzerindeki akış yapısını önemli ölçüde değiştirmektedir. Temel kanat yüzeyinde yüksek hücum açılarında görülen odak noktalı büyük ölçekli girdap, üç boyutlu yüzey ayrılmasının bir göstergesidir ve bu çalışmanın sonuçlarında pasif akıtmanın bu ayrılmayı ortadan kaldırabileceği görülmüştür.

Yüzey kenarındaki vortisitenin ve emme basıncı katsayısı $-C_p$'nin büyüklüğündeki önemli artışlar, hücum kenarı vorteksinin düzeldiğinin göstergesidir. Arka açının (β) akış yapısına etkisi göz önüne alındığında, β = 23 derece arka açılı pasif akıtma kanadı, üç boyutlu yüzey ayrımının ortadan kaldırılması açısından genel akış modeli üzerinde en üst düzeyde iyileşme sağlar. Bunun yanı sıra, belirli bir saldırı açısı için β = 18 derece arka açılı pasif akıtma kanadı da β = 23 derece ile elde edilen sonuçlara oldukça benzer ilerlemeler göstermektedir.

Anahtar Kelimeler: Düşük ok açılı delta kanat, düşük ok açısı, hücum kenarı girdabı, üç-boyutlu akış ayrılması, pasif akış kontrolü, akıtma

To my family

ACKNOWLEDGMENTS

TABLE OF CONTENTS

LIST OF FIGURES

FIGURES

LIST OF TABLES

TABLES

NOMENCLATURE

Greek Symbols

α	Angle of attack
β	Back angle
Λ	Sweep angle
ρ	Fluid density
v	Fluid kinematic viscosity
ω	Vorticity
ω_i	Uncertainty estimate of a variable i

Latin Symbols

C	Chord length
C_p	Dimensionless pressure coefficient
N	Number of samples in a measurement
p	Surface pressure
$\bar{p}$	Average pressure
p_∞	Static pressure of the flow
p_{dyn}	Dynamic pressure of the flow
PIV	Particle Image Velocimetry
Re	Reynolds number
U	Free stream velocity
u	Streamwise velocity
u_i	Relative uncertainty estimate
V	Velocity vector
w	Vertical velocity

CHAPTER 1

INTRODUCTION

In recent years, researchers pay a great attention to the studies related with flow control over non-slender delta wings, which can be considered as simplified planforms of Unmanned Air Vehicles (UAV), Unmanned Combat Air Vehicles (UCAV) and Micro Air Vehicles (MAV). Common examples of these vehicles are represented in Figure 1-1. Because aerodynamics play an important role in the flight performance and stability of an air vehicle, design parameters need to be improved; thus, researchers aim to understand and control flow physics around the delta wings. Although the early studies on aerodynamics of delta wings were conducted more than a half century ago, there is still much more topics to enlighten [1]. The most attracting part is exploring the effective methods to control the complex flow structure around the delta wings in order to prevent the instabilities introduced by different flight conditions [2].

The main classification of delta wings are performed according to their sweep angles: delta wings having sweep angle greater than 55° are called as slender (or, high swept) while delta wings having sweep angle between 35° and 55° are known as non-slender (or, low swept) delta wings. The geometry and sweep angle of a typical delta wing are represented in Figure 1-2. In the literature, there are many studies focusing on the slender delta wings, whereas considering the non-slender delta wings, very little effort has been devoted and the flow control have not been thoroughly resolved and need to be studied further.

The flow around a delta wing is dominated by two counter-rotating leading edge vortices, which are generated by the separation of the flow from the windward side of the leading edges and appear above the suction side of the wing [3]. With this continuous separation and shedding, flow rolls up into a curved free shear

1

layer, as shown in Figure 1-3. The streamwise core velocity can reach four-to-five times greater than the free stream velocity due to low pressures at the vortex core, represented in Figure 1-4. These high velocities generate an additional lift, called as vortex lift and increase the critical angle of attack [4]. However, the vortex lift contribution increases with increasing sweep angle; thus, for non-slender delta wings, it is a smaller portion of the total lift. Moreover, for non-slender delta wings, a dual primary vortex is observed on the wing surface, which is believed to be generated by the interaction of the vortical structure with the boundary layer [5].

Because of different flight conditions, vortices become unstable and some undesired formations can be observed. Increasing angle of attack may introduce several instabilities like vortex breakdown, shear layer instabilities, vortex wandering, and helical mode instability [1]. A representation of vortex breakdown and shear layer instability is shown in Figure 1-6. Among all of these instabilities, vortex breakdown, sudden expansion of the vortex core, becomes prominent due to its effects on flow structure and stability. During vortex breakdown, as represented in Figure 1-5, jet-type velocity profile at the axial vortex core turns into wake-type velocity profile because of swirl level and pressure gradient [6],[7], which in turn causes buffeting on the wing surface due to high velocity fluctuations.

Recent investigations reveal that reattachment of the separated shear layer is one of the main source of high velocity fluctuations for non-slender wings. [8]. As indicated in Figure 1-7, reattachment of shear layer demonstrates differences in slender and non-slender wings. For slender delta wings, the shear layer cannot reattach to planforms except for very low attack angles, whereas for non-slender wings, the location and strength of reattachment is quite crucial in terms of sustaining vortical coherence. The location of reattachment moves inboard with increasing incidences, and vortex breakdown proceeds through the apex of the wing. When the vortex breakdown reaches to the apex, reattachment line is located over the wing root chord, resulting substantial amount of buffeting at pre-stall region. Thus, the reattachment is the main cause of buffeting in non-slender delta wings rather than the vortex breakdown in slender wings [8].

At sufficiently high angle of attacks, where the pre-stall regime occurs over non-slender delta wings, large-scale, three-dimensional surface separation dominates the flow field. This flow regime is correlated with a large-scale, inward-swirling surface streamline pattern, which eventuates in a stable focus, as represented in Figure 1-8. The most significant feature of the three dimensional separation is the large-scale focus that streamlines emerge [45]. At the center of this focus and downstream of the leading edge, the velocity magnitude abruptly decreases, meaning that leading-edge vortices are eradicated. If the angle of attack increased further, the shear layer reattachment becomes impossible, and flow field described as a whorl, expressing that flow is stalled, and resulting very low velocity fluctuations on the planform [8].

In order to prevent these instabilities in achieving stable flight conditions, delta wings are needed to be controlled either actively or passively. These control methods aim to prevent separation, delay vortex breakdown and three-dimensional surface separation/stall, and enhance reattachment. To achieve these purposes, active control methods utilize some energy input in order to blow or suction the air on planform surface, or create steady or unsteady excitations to flow domain. On the other hand, in passive control, no energy input is required because passive control methods utilize geometry and material modifications, and in this study, a passive control method, which is called as "bleeding", is applied.

1.1 Motivation of the Study

Micro Air Vehicles (MAV), Unmanned Combat Air Vehicles (UCAV) and Unmanned Air Vehicles (UAV) are exposed to complex flow structures during steady and unsteady flight conditions. In order to improve and stabilize flight performance, lift force should be increased while buffet loads should be diminished. Because three-dimensional separation eradicates the vortical structures and induces velocity fluctuations on wing surface, it causes the elimination of vortex lift contribution and increases the buffet loads on planform. Therefore, to eliminate the three dimensional surface separation/stall, and control the reattachment location, different active and passive flow control methods have been utilized. The passive bleeding is a method, which uses simple passages

inside the wing and allows the fluid flow from the pressure side to the suction side using the inherent pressure difference.

Recently, Celik et al. [9] have developed and implemented a passive bleeding technique on 45 deg swept delta wings which have different hole orientations, called as Back (B), Edge (E) and Back & Edge (BE) referring to direction of the bleed air. In Figure 1-9, the results of surface pressure measurements, surface and cross flow visualizations and constant contours of non-dimensional vorticity measurements at Reynolds numbers $Re = 3.5 \times 10^4$ and 10^5 are represented for planforms Base and B at a high angle of attack, $\alpha = 16°$. The left column of the figure represents the results for Base wing, whereas the right column represents the results of the planform B. Considering the Base planform, the surface and cross flow visualizations demonstrate a dispersed flow on the wing surface where the traces of reattachment appear close to the symmetry line. $-C_p$ distribution indicates a flat-like shape and the cross flow patterns have very low vorticity magnitudes, which are the indications of three-dimensional surface separation. Considering the planform B, the $-C_p$ distribution has a hump-like pattern where the patterns of vorticity demonstrate 90 % increase in the maximum level of constant vorticity contours compared to the Base planform. These findings could be interpreted as the recovery of vortical structure over the planform and the eradication of three-dimensional surface separation/stall with bleeding configuration of planform B, which has bleeding holes with back angle, while no improvement were reported for the other planforms with bleed air orientations as Edge (E) and Back & Edge (BE). In consideration of the results of that study, to broadly investigate the effect of back angle and generalize the statement that the bleeding with back angle improves the flow structure in pre-stall/stall regimes, further investigations, in which the only control parameter becomes the back angle of the bleeding holes, are needed. Thus, the main motivation of this thesis is further observing the effect of bleeding with different back angles on flow structure for non-slender delta wings.

1.2 Aim of the Study

This study aims to control the flow over a 45 deg swept delta wing by utilizing passive bleeding method. In that method, control process is accomplished by inherent pressure difference between pressure and suction sides of the planform by allowing high-pressure air to the suction side in backward direction through the holes on wing surface with different back angles. In order to explore the effect of that method, surface pressure and near surface Particle Image Velocimetry (PIV) measurements were conducted in a low speed wind tunnel. Wide ranges of Reynolds numbers and attack angles, varying from $13° < \alpha < 23°$ and $3.5 \times 10^4 < Re < 12.5 \times 10^4$ were tested on bleeding configurations including three different back angles, β = 13, 18, and 23 degrees, and a Base planform.

1.3 Structure of the Thesis

This thesis is composed of five main chapters. Chapter 1 provides information on delta wings on an introduction basis and gives a brief idea about the aim and the motivation of the current study.

In Chapter 2, the literature survey including the general flow structures of delta wings are described with particular emphasis on non-slender delta wings. In addition, the flow control strategies are summarized and the passive bleeding is explained in detail.

The technical details of the experimental set-up and the measurement systems used in the study along with the experimental matrix are explained in Chapter 3.

Chapter 4 presents and discusses the results of passive bleeding experiments including the measurements of surface pressure and near surface PIV.

Chapter 5 provides the conclusions throughout the study including the recommendations for possible future work.

Figure 1-1 Representation of different non-slender delta wing types [4].
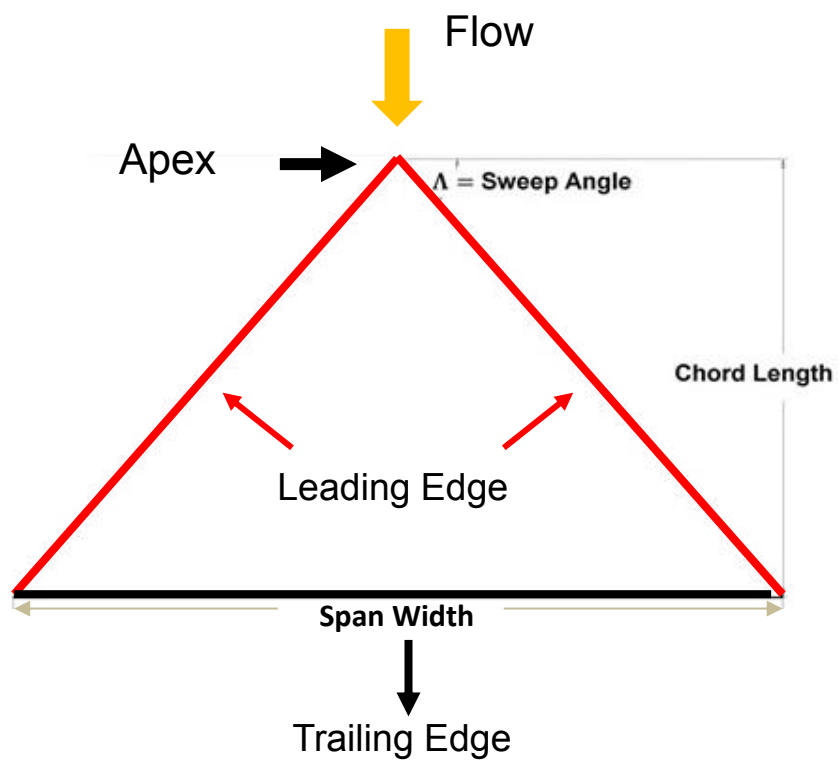
Figure 1-2 A simple delta wing geometry.
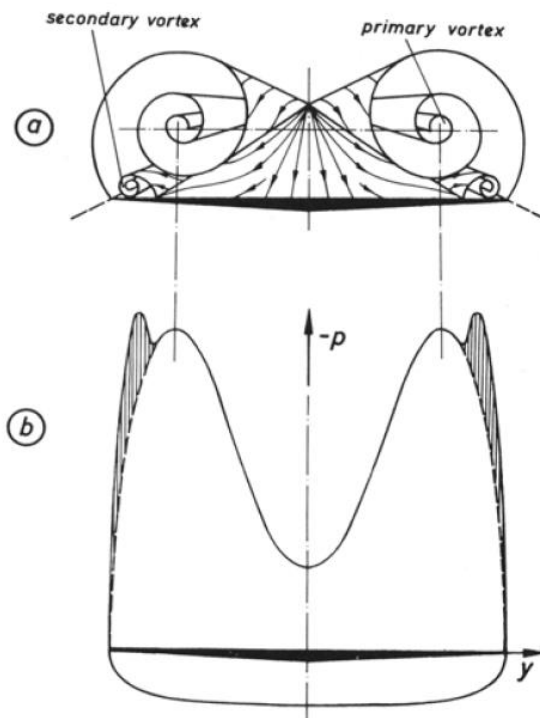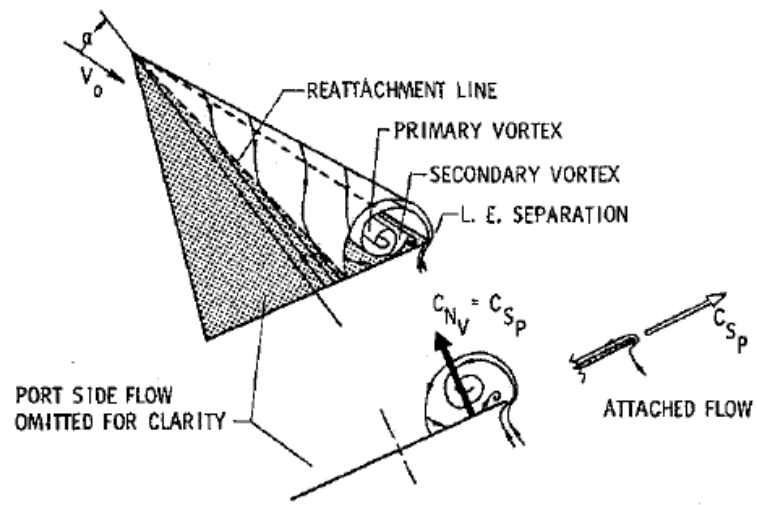
Figure 1-3 Schematic representation of shear layer and leading edge vortices over
a delta wing [11][64].
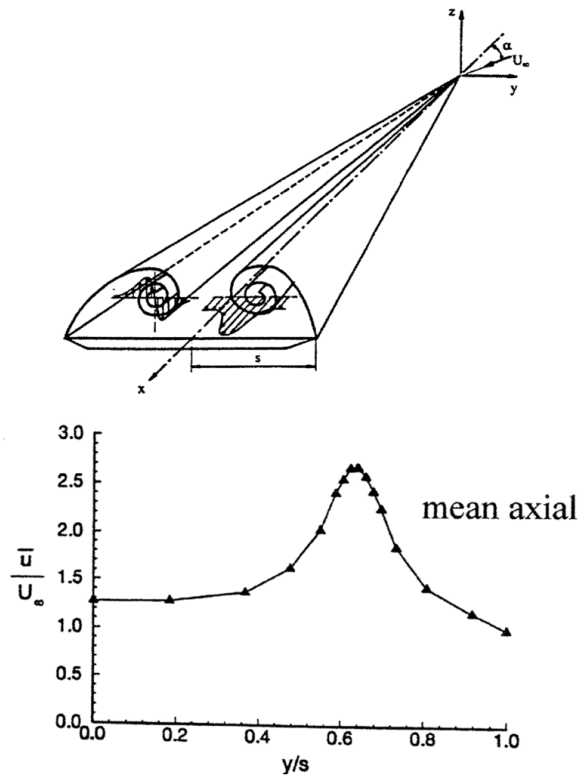
Figure 1-4 Schematics demonstrating increase in axial core velocity (top) and non-dimensional mean axial core velocities(bottom) [4].
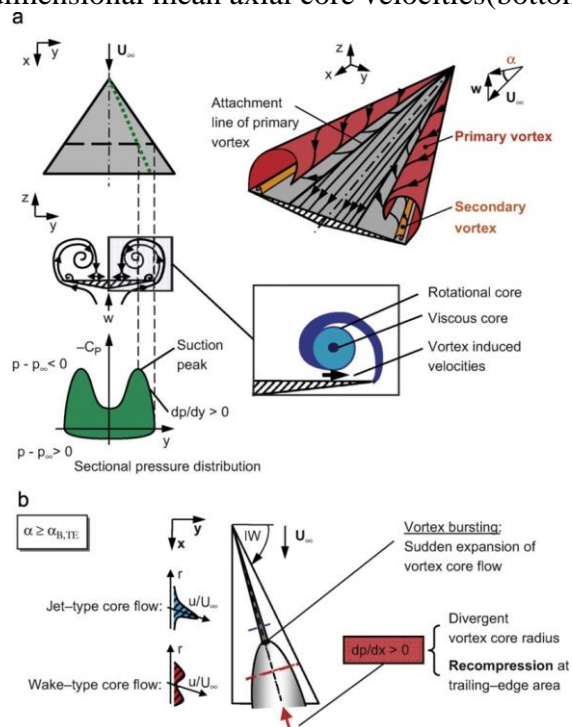
Figure 1-5 Delta wing vortex formation: main delta wing flow features (a) and vortex bursting characteristics (b) [6].
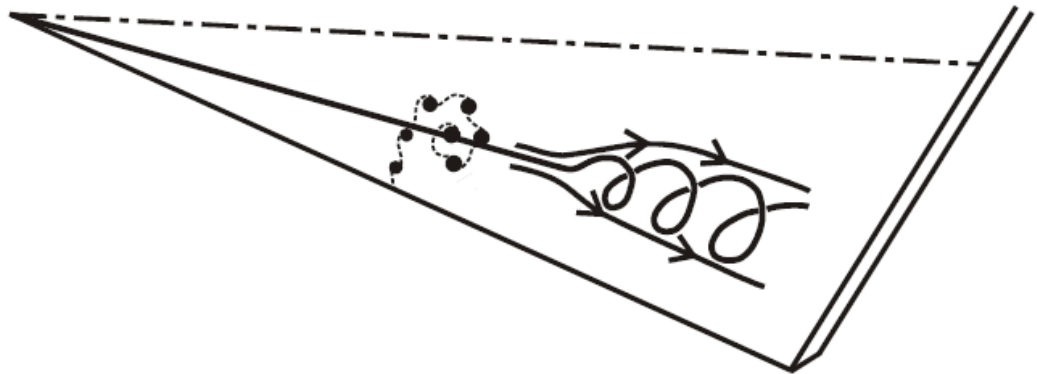
Figure 1-6 Illustration of vortex breakdown and shear layer instabilities [3].
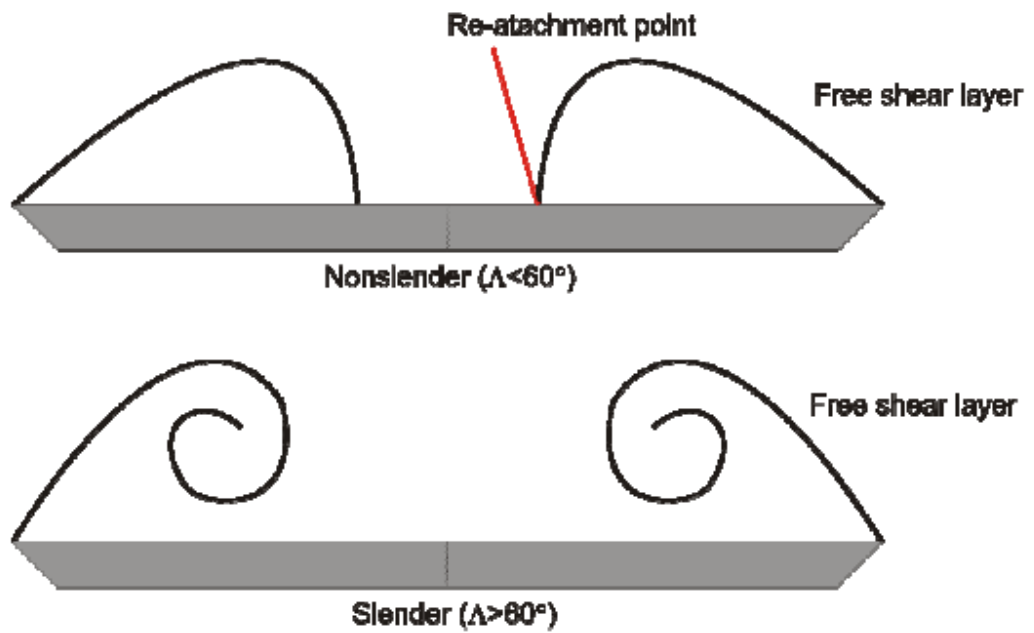
Figure 1-7 Schematic streamline patterns for (a) reattachment over non-slender wings and (b) with no reattachment on wing surface on slender [30].
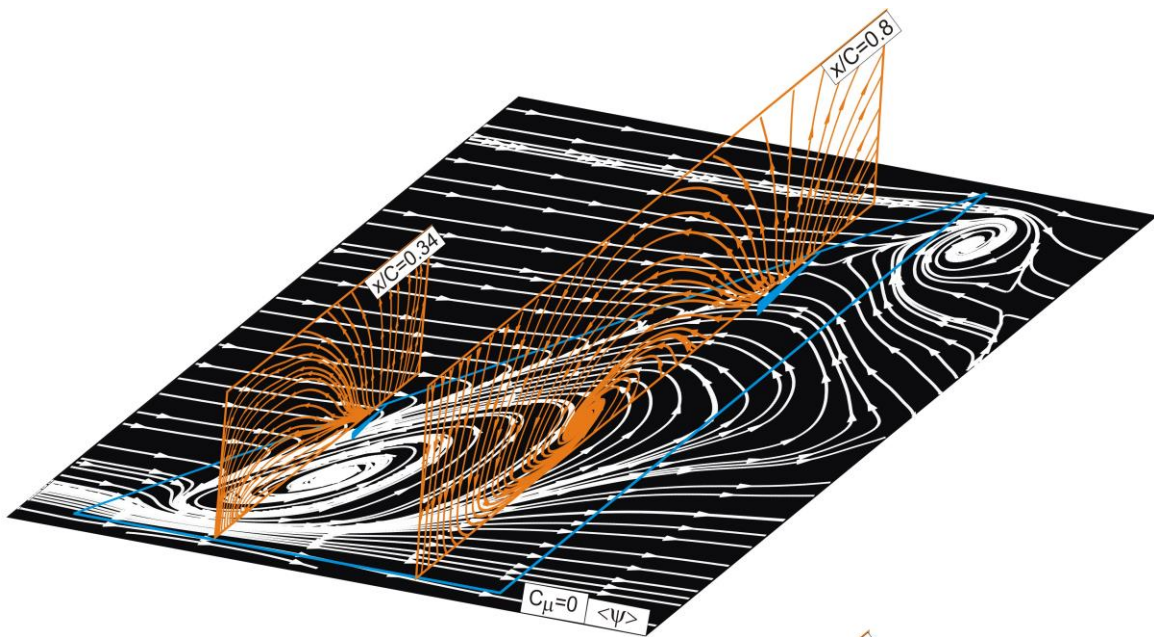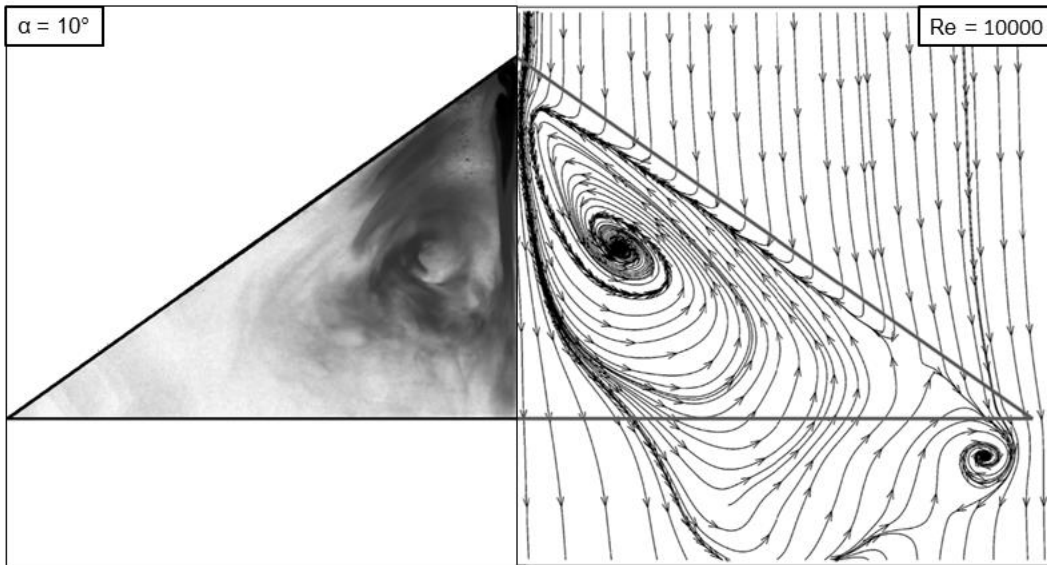
Figure 1-8 Representation of a large-scale, inward-swirling surface streamline pattern, representing three-dimensional surface separation [45].
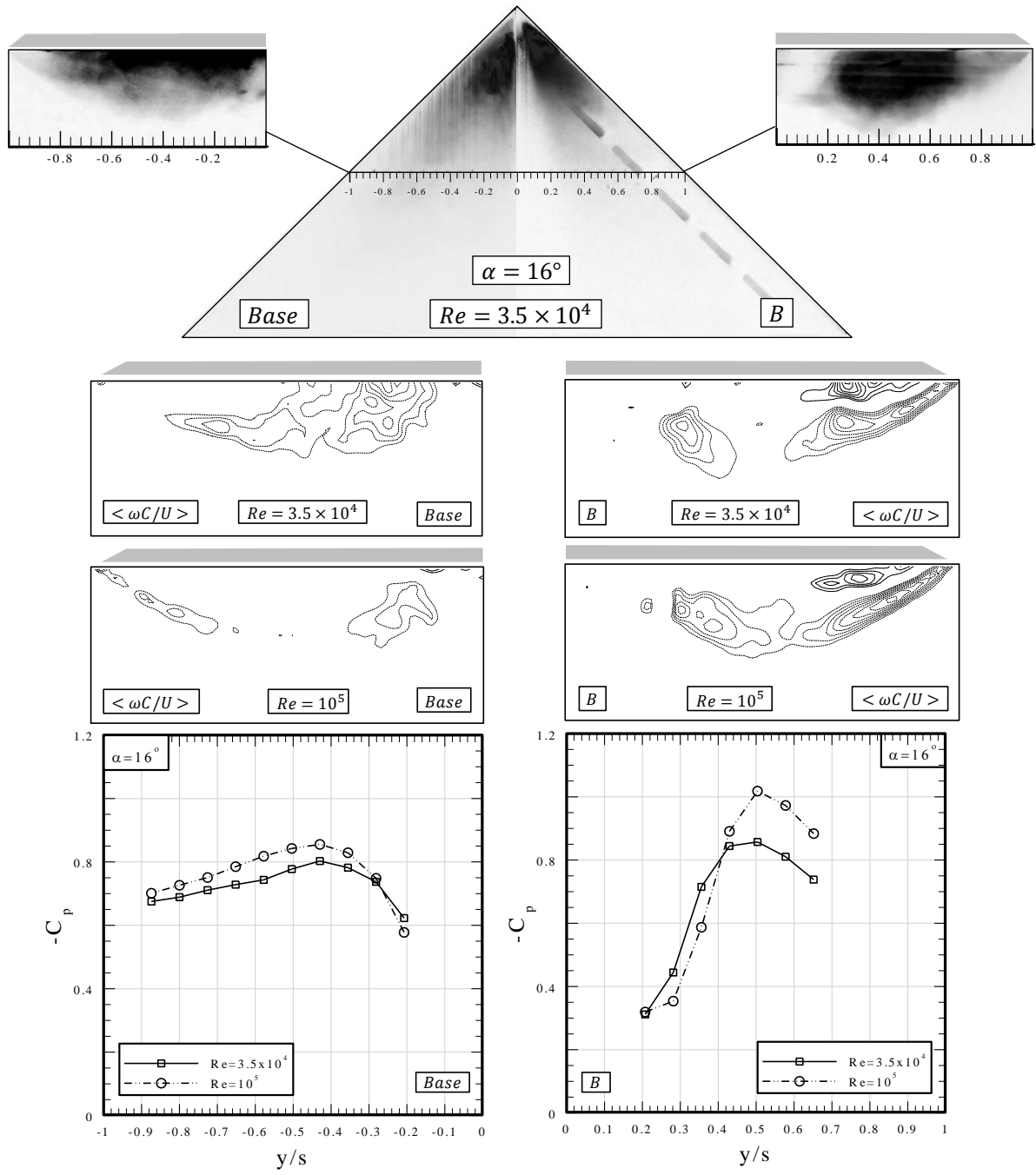
Figure 1-9 Comparison of surface and crossflow smoke visualizations at $Re = 3.5 \times 10^4$ with constant contours of nondimensional axial vorticity patterns $< \omega C/U >$ and $-C_p$ distribution at $Re = 3.5 \times 10^4$ and $Re = 10^5$ for Base (left) and B (right) planforms [9].

CHAPTER 2

LITERATURE SURVEY

In this chapter, the literature related with high and low swept delta wings is summarized. In literature, there are much more studies related with high swept delta wings than low swept case, and the main focus of this chapter is flow physics over delta wings and the flow control mechanisms, especially passive bleeding.

2.1 Flow Structure on Delta Wings

2.1.1 Vortex Structure

Flow over delta wings is dominated by two counter rotating vortices, which are formed by rolling up of vortex streets separated from leading edge of the wing over the suction side, as represented in Figure 2-1 [10]. The time averaged axial velocities at the core of these vortices may reach up to 4-5 times greater than the free stream velocity [11]. Because of the Bernoulli's principle, an increase in velocity will result a decrease in pressure at the same location; thus, the pressure will decrease at the suction side of the wings, where these vortices and high velocities are observed. Hence, these vortical structures increases the lift force on wing surfaces because they create additional lift by decreasing the pressure at suction side. According to Polhamus, the contribution of the vortex lift to the total lift force on the wing surface can be as large as the potential lift for high swept delta wings, as can be seen in Figure 2-2 [12].

Although the both have vortex formation on their suction sides, high and low swept delta wings have some major differences related with the flow structures over them. One of these obvious differences is related with the distance between

planform surface and vortex core: it is smaller for non-slender wings compared to slender planforms. The difference affects the flow structure considerably. Because the vortex core is closer to wing surface, there occurs an interaction between boundary layer and the primary vortex, forming a second vortex structure rotating in the same direction [13,14,15,77]. This formation, which is comprised of two vortices rotating in the same direction, is called as "dual vortex structure" and it can be only observed for low angle of attacks and low Reynolds numbers [16], as shown in Figure 2-3. The first study focusing on that structure was conducted by Gordnier and Vibal [5], and followed by Yanıktepe and Rockwell [14] and Taylor et al. [13] as Particle Image Velocimetry (PIV) studies. Moreover, according to Jin-Jun and Wang [15], the range of incidences with dual vortex structure becomes narrower with increasing sweep angle.

2.1.2 Shear Layer Instabilities

According to viscous flow theory, when the flow contacts with a surface, separation occurs due to the adverse pressure gradient. After flow separates from the leading edge of the delta wing, boundary layer theory loses the validity. Separated flow rolls up into a core, which is formed in three different regions: free shear layer, rotational core, and viscous subcore, as represented in Figure 2-4 [23]. Yanıktepe and Rockwell [14] classified the vortex flow as large scale patterns and small scale patterns, and the instabilities are related with the small scale patterns. The generation of these smaller vortices are caused due to Kelvin- Helmholtz instability. Moreover, Yavuz et al [19] represented sub-structures created on shear layer by using PIV technique. As shown in Figure 2-5, small scale fluctuating structures are present throughout the leading edge of the planform. Gordnier and Visbal [5] worked on the underlying causes of these instabilities. According to them, shear layer instabilities are created due to the interaction of the primary vortex structure with the boundary layer, resulting with movements of vortex core around the mean direction, which is called as vortex wandering.

2.1.3 Vortex Breakdown

At sufficiently high incidences, vortical structures over the planforms suddenly expand, and this situation is called as vortex breakdown [7]. As a result of this expansion, jet-like axial core flow stagnates, and finally, takes the form of wake-like flow and velocity at the core drops dramatically [3]. Because of the decrease in velocity, pressure increases at the suction side, which decreases the lift and momentum coefficients dramatically. The most common types of vortex core disruptions can be counted as spiral, double helix and bubble type vortex breakdown on wing planform. Slender delta wings generally exhibit spiral type vortex breakdown as in Figure 2-6 and Figure 2-7 [11], which fluctuates along streamwise direction, while non-slender planforms have a tendency to develop a conical shape of breakdown, in which swirling in the core and reversed axial velocity are not observed [14,17,18]. The two main parameters, which affect the formation of vortex breakdown, are swirl level and external pressure gradient. Any increase in one of these parameters may cause to disrupt vortex core earlier. According to Erickson [10], the results of the experimental studies conducted in wind tunnels and water channels are well in line with the real flight conditions.

Vortex breakdown is an undesired phenomenon because of its severe effects on flow. The deterioration of vortex structure and the decrease of axial core velocity will increase the pressure at the suction side of the planform, leading a decrease in vortex lift contribution, eventually. Actually, the most important consequence of vortex breakdown is high buffeting loads exposed to planform, which eventually leads to structural vibrations and fatigue damage. These consequences mean that aerodynamic performance decreases in the pre-to-post stall regimes.

2.1.4 Shear Layer Reattachment and Three-Dimensional Separation/Stall

Reattachment is one of the main characteristics of flow over delta wings because the shear layer separated from the leading edge attaches to the suction side of the wing for both slender and non-slender cases. For slender wings, reattachment is not occur on the planform, it can only attach to the surface for very small incidences [3], which is difficult to control. However, for non-slender wings,

separated flow attaches to the planform from outboard of the symmetry line, compared to slender wings [4]. A comparison of these two conditions is represented in Figure 1-7. According to Taylor and Gursul [4], increasing attack angle cause to shift the reattachment line to the inboard of the symmetry plane. The reattachment line can reach the centerline of the just prior to the stall, for $\alpha \approx 22 - 23°$, after vortex breakdown reaches to the apex. In that case, high velocity fluctuations in the symmetry plane is observed, meaning that the main cause of buffeting is the shear layer reattachment, rather than vortex breakdown in the pre-stall regime [8].

At sufficiently high angle of attacks, in which case the pre-stall regime occurs over non-slender delta wings as shown in Figure 2-8, the vortical structure gives place to the large-scale, three-dimensional surface separation over the planform. This flow regime is governed by a large-scale, inward-swirling surface streamline pattern, which eventuates in a stable focus, which is the most significant feature of three-dimensional separation. Hornung and Perry [68] referred this as Werlé–Legendre separation, in which the flow rolls up into a focus. In Figure 2-9, the structure of three-dimensional separation is represented: the saddle of separation initiates the separation process through a bipartition. One of the ends of this bipartition rolls up and culminates into a focus, whereas the other end proceeds through the downstream [73].

For further increase of attack angle ($\alpha = 25°$), as shown in Figure 2-8 streamlines takes the form called as whorl, which means that stall condition occurs and in that case, shear layer can no longer reattach to the planform surface, resulting low velocity fluctuations and buffet loads [8]. Thus, it is important to control the flow in order to delay stall, enhance lift and prevent buffet loads, also re-formation of reattachment over non-slender planforms in the post-stall regimes.

2.2 Flow Control Techniques on Delta Wings

In order to have stable flight conditions, the aforementioned instabilities are needed to be prevented; in other words, delaying stall, separation, vortex breakdown and eliminating buffet loads by regulating flow reattachment in a

desired manner are necessary. For slender delta wings, the main focus of the control strategies is preventing the vortex breakdown, while in non-slender delta wings, the reattachment line is needed to be regulated. The flow over delta wings can be controlled in two manners: actively or passively. In literature, Gursul et al. [3] have extensively reviewed the active and passive control techniques for slender and non-slender wings. In active control, an energy input is required: in blowing and suction of air from edges or surfaces of the planforms, controllable flaps, and small and large scale perturbations [3]. However, the passive control methods do not require any energy input because they generally adjust the flow by changing the geometrical and material properties of the wings. As common examples to this technique, flaps, elastic materials attached on wing surface, modification on leading and trailing edges can be counted [21,22,25,61,80].

2.2.1 Active Control

Active flow control in delta wings are very popular and a great attention have been paid for several years to explore new techniques. One of the most common method that has been used in that field is a pneumatic technique, which is controlling the flow by suction and blowing. In this method, leading edge vortices can be controlled with the help of leading edge blowing or suction [26,27-31], trailing edge blowing and suction[32-34], and along core blowing and suction techniques [35-37,3,81] and they can be applied in steady or unsteady manner, but unsteady blowing is more effective than the steady blowing [3]. As an example of leading edge blowing, Wood et al. [38] performed the steady blowing method thoughout the leading edge for a $\Lambda = 60°$ sweep delta wing and found that vortex structure can be controlled up to $\alpha = 50°$. McCormik and Gursul [39] and Badran [40] applied the leading edge suction to high swept delta wings and showing that this method can move vortex breakdown to downstream and affect the vortex core location in a good manner. Gursul [3] studied the along core blowing method and represented that it is the most effective technique among the others in terms of vortex breakdown location control. Also, that method accelerates the axial core flow and favorably adjust the pressure gradient [41]. In addition to along core blowing, trailing edge blowing is also effective in terms of vortex breakdown

17

delay according to the study, which applied that method to a $\Lambda = 60°$ sweep delta wing [42].

Although there are excessive amount of study applying these control methods to the slender planforms, this is not the case for non-slender delta wings. Wang [43] conducted an important study to control non-slender wings, by applying a trailing edge blowing and concluded that it is difficult to control the vortex breakdown location and postpone its occurrence for these planforms. Zharfa et al. [44] concluded their study that steady blowing is an effective way to control the occurrence of three-dimensional separations from a $\Lambda = 35°$ sweep delta wing. Moreover, Yavuz and Rockwell [33,45] performed a characterization study for $\Lambda = 35°$ sweep delta wing to understand the near surface topology when applying the steady trailing edge blowing method.

In terms of unsteady blowing and suction studies, Guy et al. [46,47], Gu et al. [26], Gad-el-Hak and Blackwelder [48] performed experimental studies to show the effect of periodic suction and blowing along the leading edges of slender planforms. The main conclusions of these studies represented that lift can be improved while stall and vortex breakdown can be delayed with the help of these techniques. The effectiveness of these methods are represented in Figure 2-10.

In addition to the suction and blowing methods, some researchers control the flow structure over the delta wings by applying oscillatory motion to the wing. Yanıktepe et al. [14] and Vardaki et al. [82] applied oscillatory motion at post-stall regime while Yavuz et al. [19] applied at pre-stall regime to control reattachment. They concluded that oscillatory flow promotes reattachment in low-swept delta wings. As represented in Figure 2-11 with the help of oscillation, totally separated flow reattaches to the surface.

2.2.2 Passive Control

Despite the active control, passive control methods do not require any energy input because they utilize the effects of geometrical and material modifications. Although they are simpler and cheaper than active control methods, sometimes they may be concluded with unexpected results.

18

Because the purpose of controlling the flow is different for slender and non-slender planforms, the applications are different. For slender wings, the main purpose of control is postponing the vortex breakdown and adjustion its position on planform. Klute et al. [49], Gursul et al. [50] and Mitchell et al. [51] studied the effects of apex flaps, leading edge flaps and extensions over the control of vortex breakdown. The main conclusion of these studies is that the vortex breakdown can be delayed if the bended and stationary apex flap is attached to the surface of the wing. Also, the maximum delay is obtained in the case of apex flaps bended to the planform with an angle toward negative direction.

On the other hand, because the main motivation of controlling the flow over non-slender wings is the adjustment of the reattachment line, Vardaki et al. [52] and Mitchell and Delery [51] suggested the usage of flexible wings. According to their results, a delay in three-dimensional separation and an enhancement in reattachment of shear layer is obtained with the help of flexibility. Taylor et al. [21] studied the effect of flexibility by using $\Lambda = 40° - 60°$ sweep delta wings, and reported that an improvement in lift force is obtained with the help of this method.

Another important method, which is called as bleeding, is suggested in recent studies, and it requires the holes and openings in the planform surface in order to energize the flow over the wing, which is the subject of this study. Therefore, that method is needed to be investigated comprehensively.

2.2.2.1 Bleeding

In recent years, a new methodology, which is called as bleeding, arises as a novel flow control technique. In this method, inherent pressure difference between suction and pressure side is utilized, either actively or passively. One of the significant characteristics of that method is the slots, which are opened close to the wingtip, as explained by Hu [53]. With the help of these slots, air is conducted from pressure side aft to suction side fore, as represented in Figure 2-12. Indeed, bleeding works nearly in the same logic with blowing or jet injection, with some

major differences: in the bleeding method, the air coming to suction side is directed from the pressure side, rather than supplied by any other means.

In active bleeding, actuators are utilized in order to orient the slot direction and geometry. On the other hand, in passive bleeding, holes remain fixed; therefore, it is a relatively simple flow control strategy. In 1920s, Lachmann [54] tested that method on slotted wings and ailerons. Actually, the main conclusion is represented by Tanner [55], suggesting that bleeding can be utilized as a drag reduction method. In addition to the slots, porous surfaces was also studied as a bleeding method. Bauer and Hemsch [56] experimentally studied passive porosity on tangent-agive forebodies and showed that porosity eliminates the asymmetric forces. In their numerical study on tailless fighter aircrafts, Hunter et al. [57] represented that passive porosity can be utilized as a control effector. Moreover, Carpenter and Porter [58] showed that passive porosity is a good method in controlling boundary-layer instabilities, theoretically. In addition to these early studies, Kearney and Glezer [59] studied bleeding on two dimensional VR-7 airfoils at 2012. The results expressed that bleeding has positive effects on aerodynamic forces and moments. Moreover, Hu et al. [53] also concluded that different slots geometries can be utilized to eliminate roll oscillations without any negative effect, and with the help of these slots, separated shear layer may again form votical structures. These important finding is supported by the experimental study of Celik et al. [9]. In that study, different bleed hole orientations was tested, which are Back (B), Edge (E) and Back-Edge (BE). According to their pressure measurement, smoke visualization and Particle Image Velocimetry (PIV) results, at angle of attack $\alpha = 16°$, where the three-dimensional separation occurred, the recovery of the vortical structures with an increase in magnitude of suction pressure coefficient is achieved with back angled bleeding configuration, as shown in Figure 1-9. Also, all configurations move reattachment line to the outboard of symmetry line. Therefore, they concluded that, bleeding might eliminate the three dimensional surface separation in low-swept delta wings while promoting the flow reattachment to the wing surface.
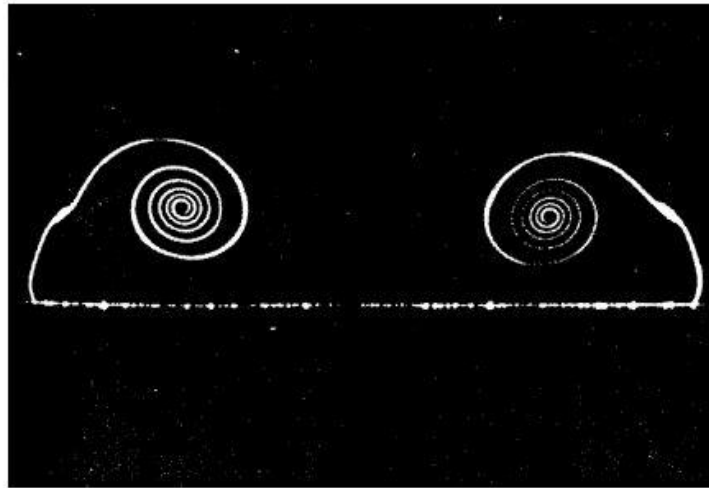
Figure 2-1 Shear-layer separaiton and formation of leading edge vortex [24].
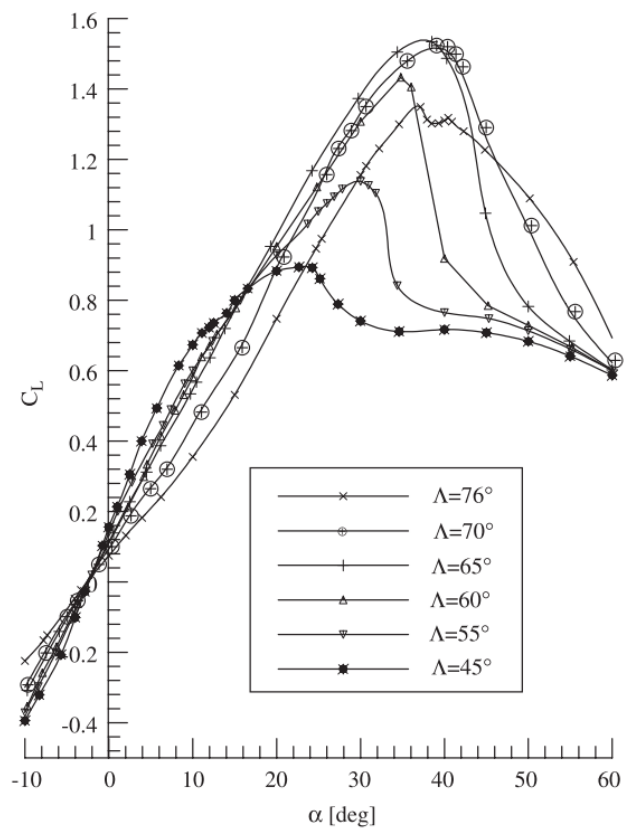
Figure 2-2 Illustration of vortex lift contribution to lift coefficient [1] .
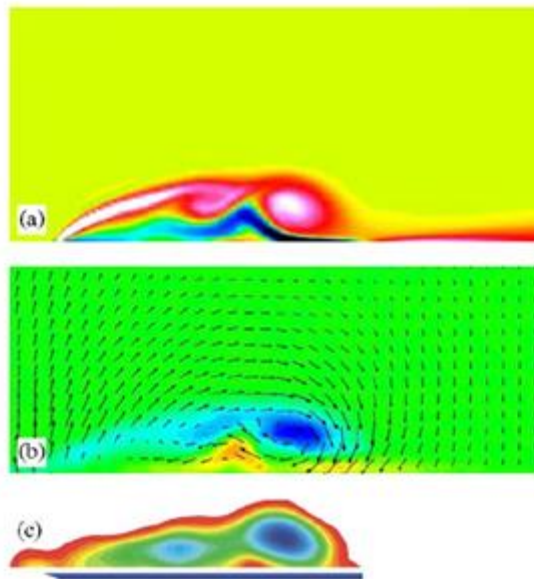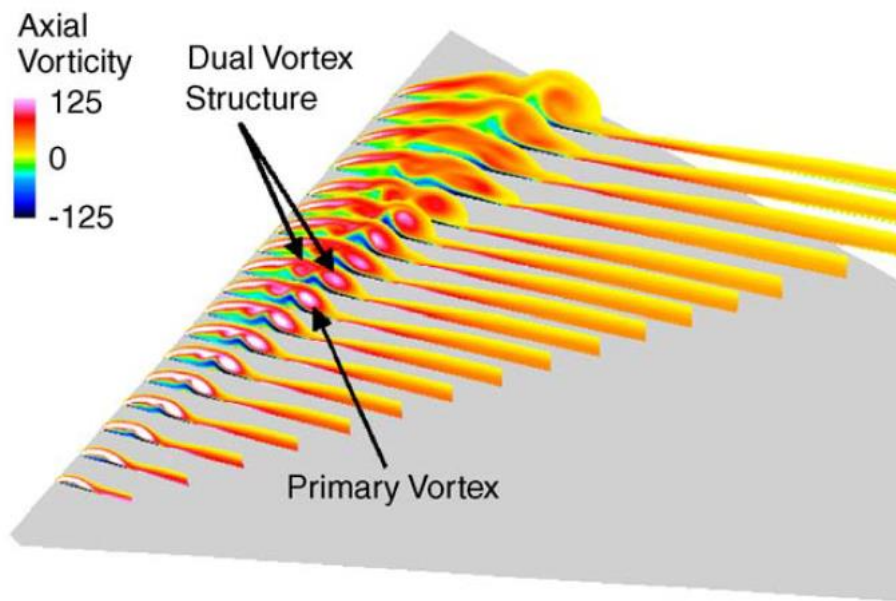
Figure 2-3 Illustration of dual vortex structure, from the studies a) Gordnier and Visbal [4], b) Taylor et al. [5], c) Yanıktepe and Rockwell [14].
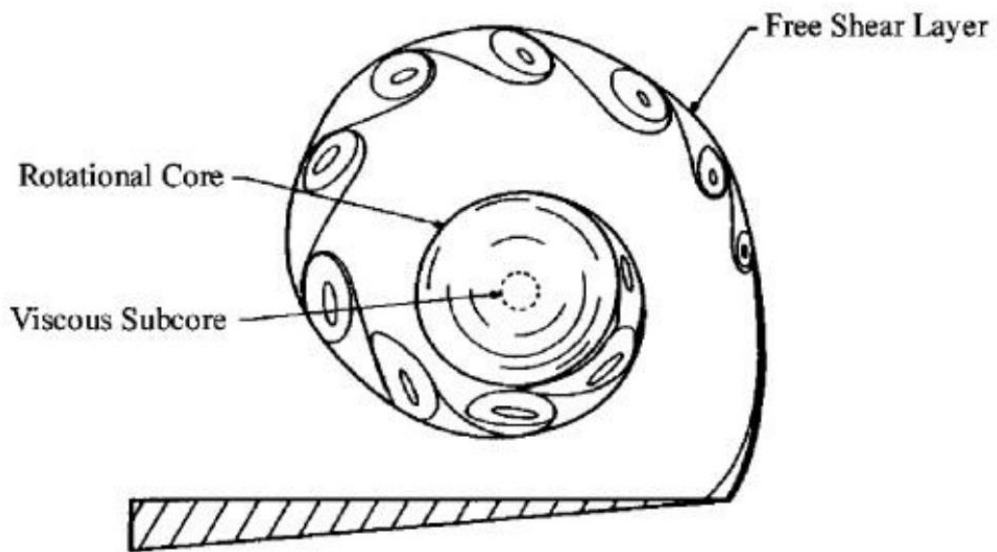
Figure 2-4 Regions of a shear layer [23].
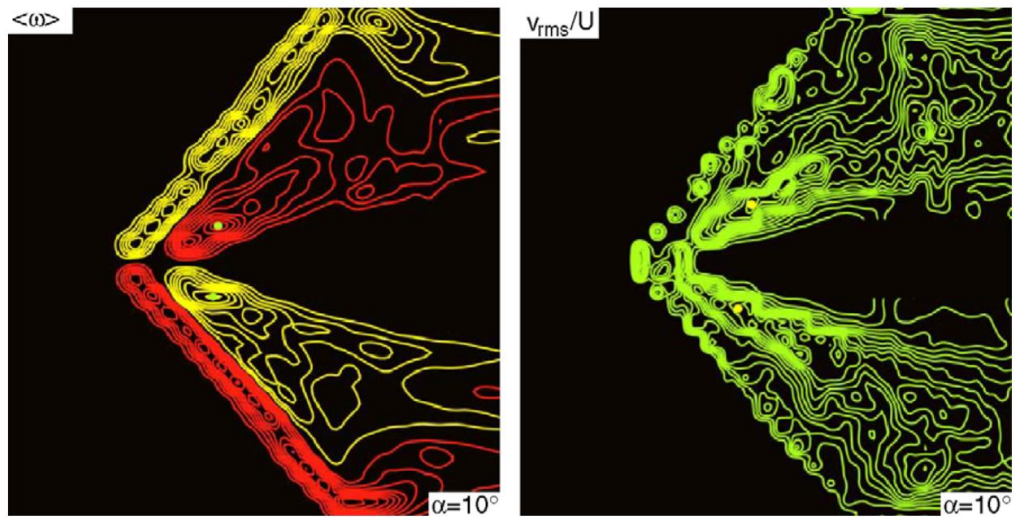
Figure 2-5 PIV measurement results of shear layer sub-structures for a 38.7 deg swept delta wing [62].
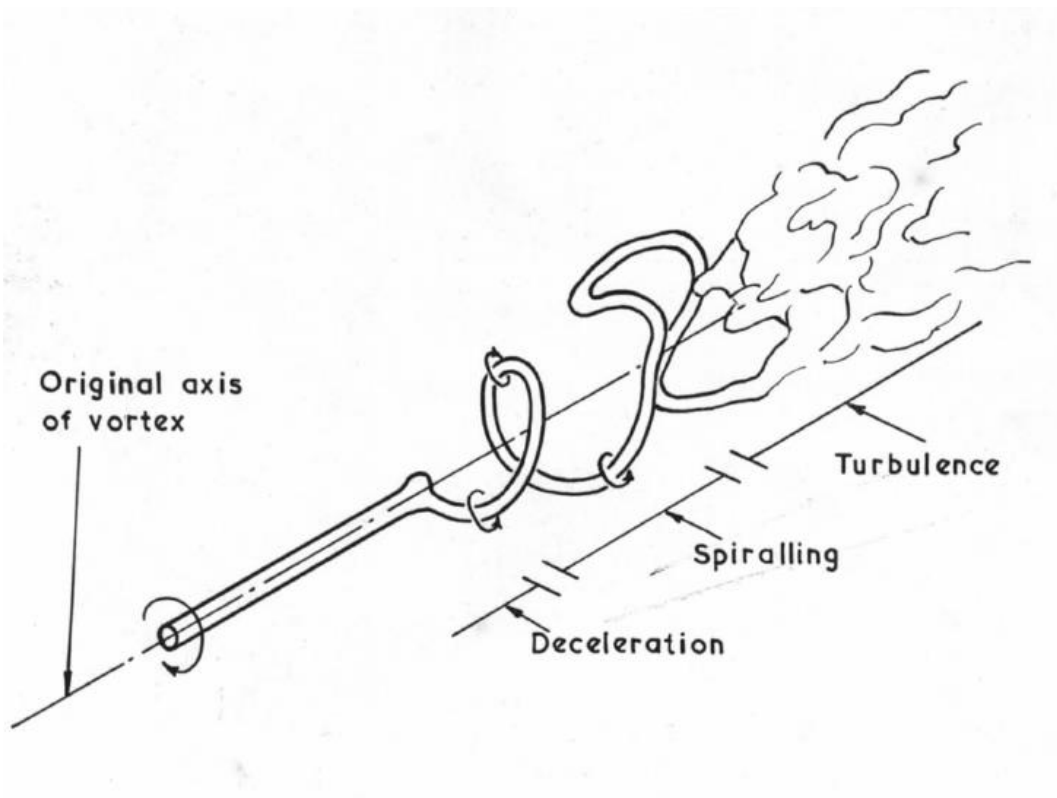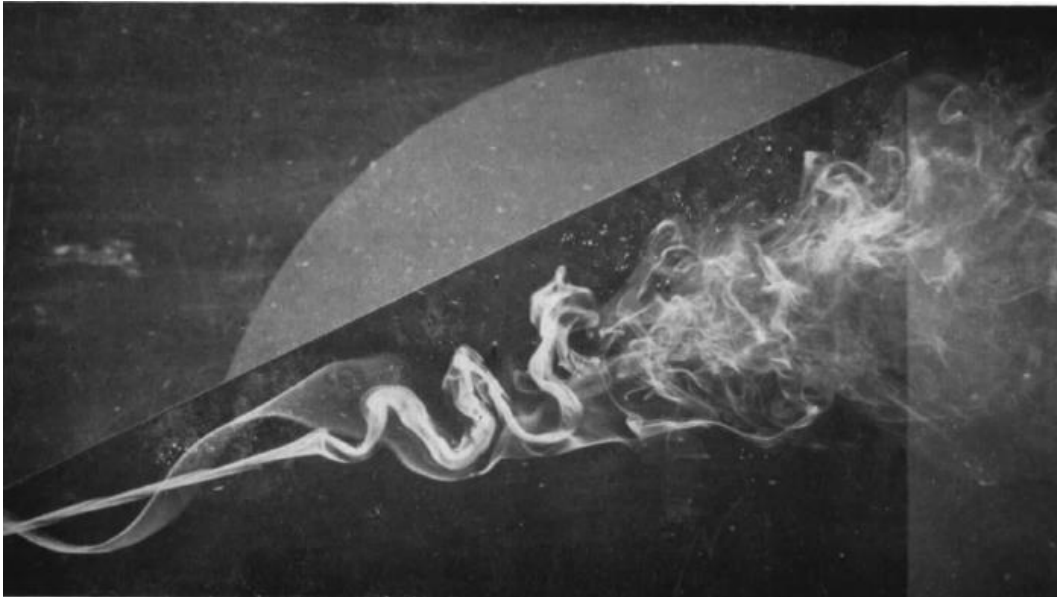
Figure 2-6 Illustration of vortex breakdown experienced by slender delta wings [11].
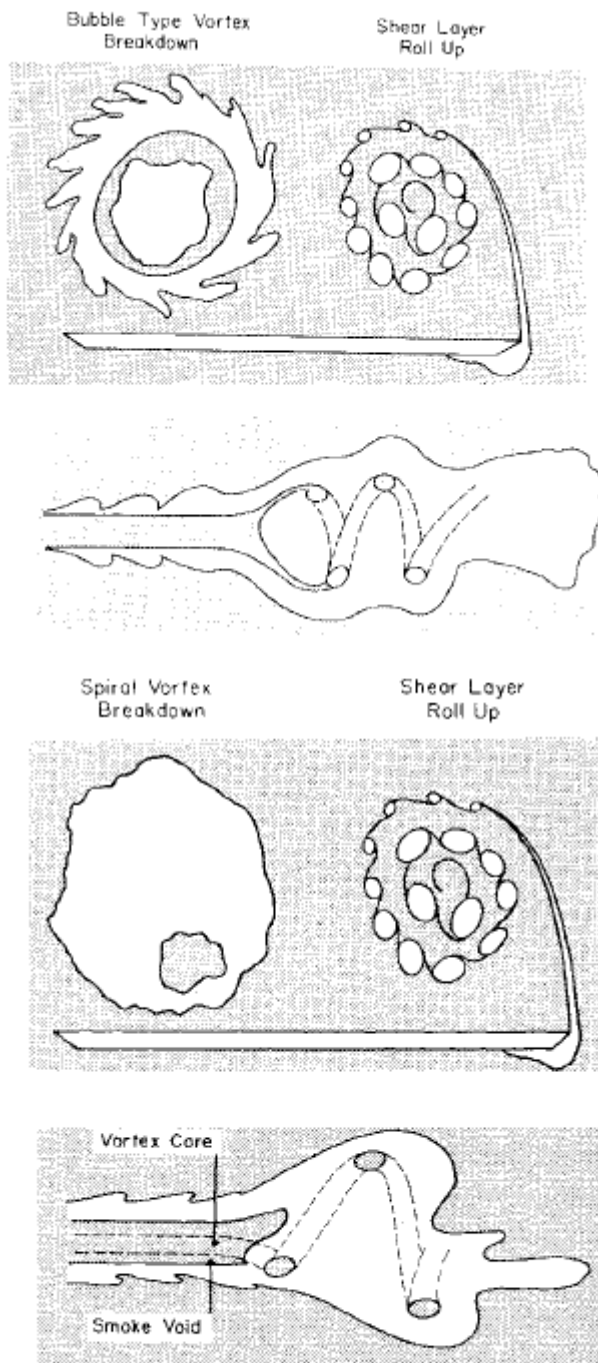
Figure 2-7 The most common types of vortex breakdown: Bubble and Spiral type [65].
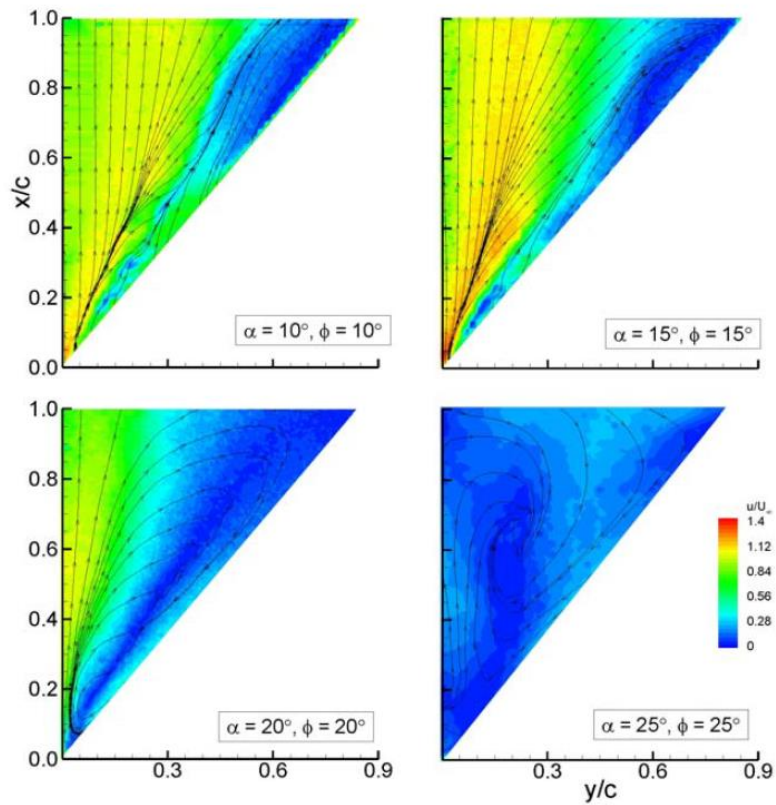
Figure 2-8 Magnitude of time-averaged velocity and streamline pattern near the wing surface: Representation of three-dimensional surface separation and stall [66].
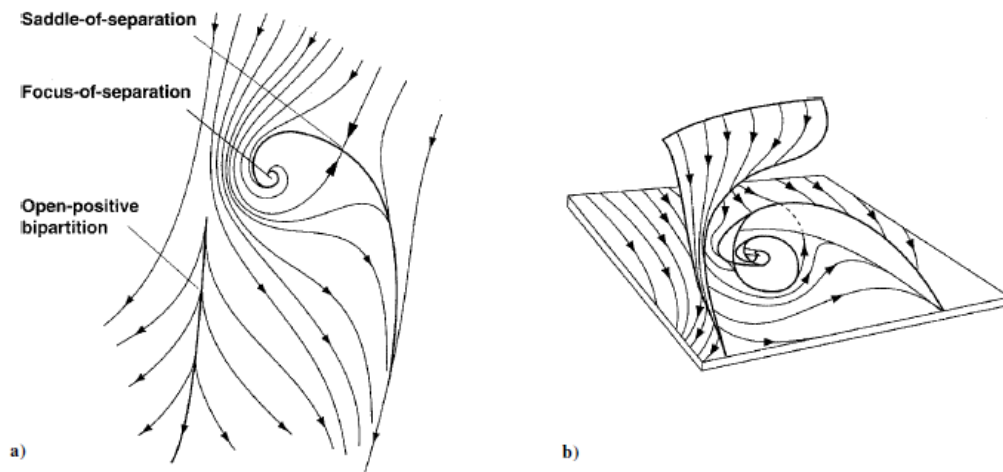
Figure 2-9 Surface and offsurface characteristics of Werlé–Legendre separation [73].
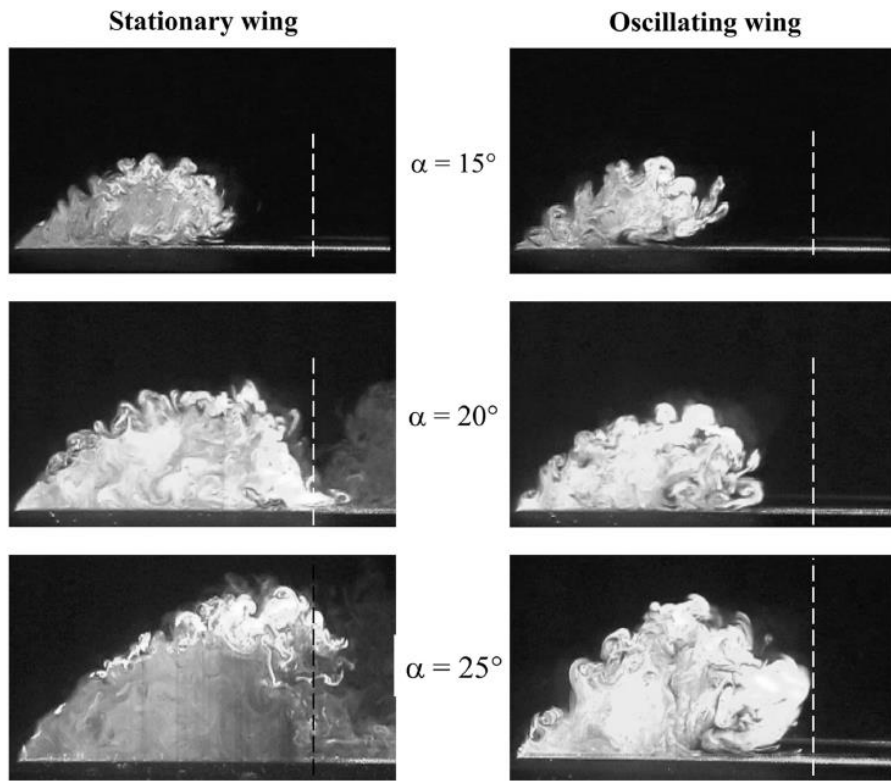
Figure 2-10 Effect of control with oscillation on reattachment location [82].
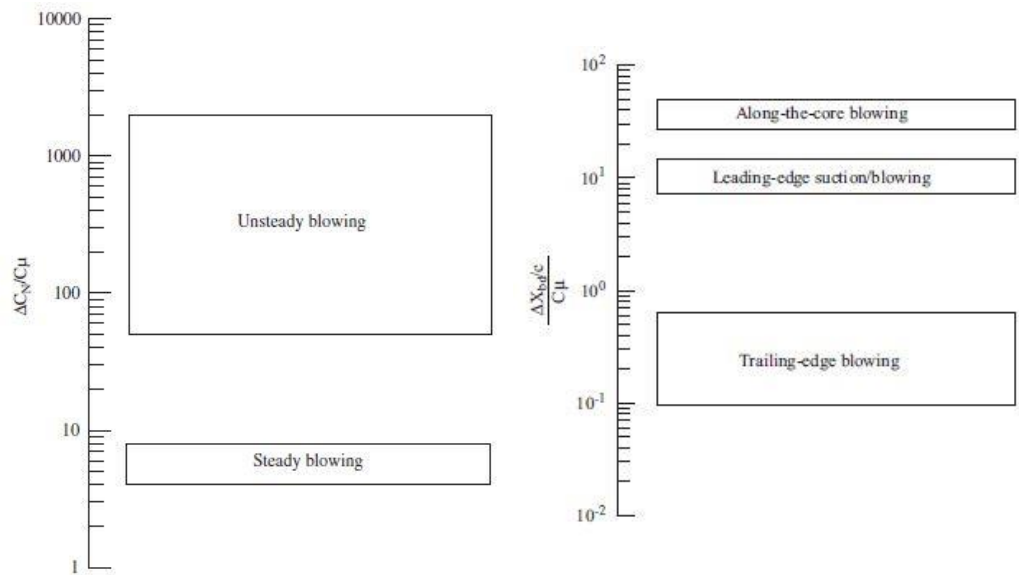
Figure 2-11 Effectiveness of (left)steady and unsteady blowing (right) blowing-suction methods [4].

Figure 2-12 Bleed through the airfoil [59]

CHAPTER 3

EXPERIMENTAL SET-UP AND TECHNIQUES

3.1 Wind Tunnel

The experiments are conducted in a low speed, open circuit and suction type wind tunnel, driven by an axial fan having 10Kw AC motor, is located in the Fluid Mechanics Laboratory of Mechanical Engineering Department at Middle East Technical University. The overview picture of the wind tunnel facility is presented in Figure 3-1.

The tunnel is composed of fine main parts: settling chamber, contraction cone, test section, diffuser and fan, respectively. At the inlet, wind tunnel has two symmetrical sections where air is introduced through the tunnel. These entrances are covered with fine mesh screens in order to make the flow uniform. Throughout the settling chamber, which is 2700 mm long and known as the entrance region of the tunnel, three more fine mesh screens and one honeycomb are located to improve the uniformity and to reduce the turbulence intensity. After the settling chamber, a contraction cone is present which is 2000 mm long and has a ratio of 8:1.

Transparent test section allows light access through plexiglass walls for optical measurement techniques and has dimensions of 2000 mm length, 510 mm height and 750 mm width. The maximum free stream velocity, which can be obtained in the test section, is 30 m/s.

Following the test section, a diffuser having a length 7300 mm is located to decelerate the flow in order to reduce the power required to drive the tunnel and to increase the static pressure.

The tests were conducted at free stream velocities $4.13 \frac{m}{s}$, $8.86 \frac{m}{s}$ and $14.76 \frac{m}{s}$ which correspond to the Reynolds numbers $Re = 3.5 \times 10^4$, $Re = 7.5 \times 10^4$ and $Re = 12.5 \times 10^4$, which are calculated based on the wing chord length, C, via Equation 3.1. These velocities are adjusted by remotely controlling the frequency of the fan with a control unit.

$$Re = \frac{U_\infty C}{\upsilon} \tag{3.1}$$

3.1.1 Wind Tunnel Characterization

The wind tunnel characterization was performed with the measurements of Laser Doppler Anemometry (LDA) and pitot-static tube, by measuring the velocity at different fan powers. The measurements were taken from one fixed point in the test section, and the average velocities of both techniques are represented in Figure 3-3, which is the tunnel calibration curve. The comparison shows that the difference between two techniques, velocity measurements with LDA technique and velocity calculations with pitot-static tube measurements, is around 3%. According to the tunnel calibration curve, tunnel power and average velocity linearly changes for the fan power larger than 4%, corresponding to a tunnel velocity $5 \frac{m}{s}$, approximately. On the other hand, a polynomial curve fit is necessary for the values smaller than that percent, because for low fan powers, losses become significant. Therefore, it is necessary to understand the uniformity of the tunnel at the low free stream velocities by conducting some tests. In previous studies [60], LDA is used for tracing the flow in test section at two low free stream velocities, and it is reported that, the maximum difference between these two low free stream velocities could not exceed 5.7%. Besides the uniformity, the concept of turbulence intensity is one of the main criterion of the performance of the wind tunnels. The turbulence intensity of the tunnel was determined by using LDA method for a wide free stream velocity range. In Figure

30

3-3, the intensity values are also plotted and at the test section, the turbulence intensities do not exceed 1%.

3.2 Flow Measurement Techniques

3.2.1   Surface Pressure Measurements

In pressure measurements, Netscanner 9116 Intelligent Pressure Scanner was used. Pressure scanner has 16 silicon piezoresistive pressure transducers, allowing to record the pressure from 16 channels within the range of 0 to 2.5kPa. Even though the scanner was calibrated over a certain pressure and temperature ranges by the supplier, the pressure measurements were conducted using a manometer prior to the experiments to confirm the calibration curves provided by the supplier. The calibration settings of each transducer were stored in the EEPROM (Electrically Erasable Programmable Read-Only Memory). With the help of integrated microprocessor and the temperature sensors, transducer outputs for offset, nonlinearity, sensitivity and thermal effects prior to transferring data to the computer are compensated. Thus, the system ensures a measurement resolution of ±0.003% FS (full scale) and accuracy of ±0.05% FS.

For all experiments, the data was recorded at a 500 Hz sampling rate for 10 seconds. The repeatability of the experiments was evaluated using different number of data sets in averaging. Initial experiments showed that averaging of three data sets supply saturated results. The detailed investigation on uncertainty analysis for the pressure measurements is reported at the end of this chapter. The noise of the environment was also measured with the same sampling rate and time,for three sets, and their average is subtracted from the data for each experiment.

The results of the pressure data were presented as dimensionless pressure coefficient values C_p, which is calculated via Equation 3.2. For the corresponding pressure distribution charts the C_p values were shown as $-C_p$ that plotted with respect to the dimensionless spanwise location of the pressure taps, y/S. The

detailed illustration of these taps are present in Figure 3-8, and Figure 3-9 shows $-C_p$ versus y/S representation for a typical leading edge vortex.

$$C_p = \frac{\overline{p} - p_\infty}{\frac{1}{2}\rho U_\infty^2} = \frac{\overline{p} - p_\infty}{p_{dyn}} \qquad (3.2)$$

U_∞ : Free stream velocity

$\overline{p}$: Time-averaged surface pressure

p_∞: Flow static pressure

ρ : Density of the fluid

p_{dyn}: Flow dynamic pressure

3.2.2 Particle Image Velocimetry (PIV) Measurements

The flow fields under the planforms were acquired by using Particle Image Velocimetry (PIV) experimental method. PIV is a non-intrusive technique, which measures instantaneous velocity field by making flow visible with the help of seeding particles, and a laser sheet to illuminate them. This laser sheet is not continuous, and its pulsation frequency enables to determine the time step. This illuminated region of interest is captured with the help of a camera. For each case, camera captures two images; the first image is called as frame 1 and captured at time t_1, while the second image is called as frame 2 and captured at time t_2, and each frame is divided into small interrogation areas, all of them having some amount of tracer particle. Thus, because the displacement Δx between two particles in the same interrogation are of two images and the time difference between first and second laser pulse Δt, the velocity of flow in the region of interest is calculated with the following formula:

$$U_\infty = \frac{\Delta x}{\Delta t}$$

TSI 2D Dynamic PIV system was used for the experiments in the study. The basic configuration of a PIV system is composed of:

- Double-pulse laser and its optical equipment (the spherical-cylindrical lens combination).
- Frame grabber
- CMOS camera
- Synchronizer
- Illuminating particles
- Computer with INSIGHT 4G.

In Figure 3-4, working principle of the PIV is shown.

Tracer particles are one of the important components of PIV system because their movements help to understand the instantaneous velocity. The seeding material is selected according to the criterions that they must be large enough to reflect the light from laser and small enough to follow the fluid. In that study, ViCount Compact 1300 oil based smoke generator aimed for wind tunnel applications were used in this study with a glycol based fog fluid.

In order to illuminate the flow field, the laser system is utilized. PIV system in experimental set-up uses Litron Nano L 200-15 PIV laser system comprising double pulsed and Q-switched Nd: YAG laser with a visible 532 nm laser light. The output energy of the laser at 532 nm was 200 mJ and repetition rate per laser head ranged between 0-15 Hz. A laser sheet was created by using a set of spherical and cylindrical lenses. In that study, near surface flow PIV experiments were conducted, and for near surface flow velocity measurement, the laser sheet was positioned parallel to the wing surface. The measurements were taken both 3 and 4 millimeters away from the wing surface.

Images of the tracer particles in the flow field and interrogation areas were captured by a digital TSI Powerview™ Plus 4-megapixel, CMOS camera with a Nikon 50 mm F1.8 lens, having 2048×2048 pixel resolution. In this study, 200 image pairs were captured for cases. A frame grabber reads and stores the images

as a digital image in the RAM of the computer. In order to synchronize the camera and the laser, a synchronizer was utilized.

Insight 4G software was used to control the PIV setup. The separation time (Δt) between two laser pulses was adjusted according to free stream velocity, U_∞. After adjusting all of these components, FFT (Fast Fourier Transform) correlation technique was performed to process the 200 image pairs. The movement of particles within interrogation areas of each frames were analyzed to obtain the average flow vector by applying cross-correlation method to analyze the displacement of the seeding particles over time. In each frame, the interrogation areas were cross-correlated pixel by pixel, with each other. After correlations were completed, Tecplot was used to examine the time-averaged streamlines $< \Psi >$, velocity $< V >$, and time-averaged vorticity $< \omega C / U >$ patterns.

The schematic representation of the PIV setup with the connections among the components is shown in Figure 3-5. For near surface flow velocity measurements, the laser sheet was oriented parallel to the planform surface. The PIV camera was located under the test section and lens surface of the camera was also parallel to the wing surface.

3.3 Delta Wing Models and Experimental Matrices

Bleeding is a technique, which uses the pressure difference between low and high pressure surfaces of the wing with the passages opened at the selected locations on the wing surface. This would allow the airflow from the pressure side to the suction side of the, which might ultimately improve the flow field depending on the geometry and locations of the holes. In previous study conducted by Celik et al. [9], three different hole orientations, namely back, edge and back-edge, were tested, and it was shown that holes having back angle improve the flow field, especially in pre-stall conditions.

In the present study, in order to extent the understanding of the effect of back angle on flow structure, three delta wings with different back angles were designed. The delta wings used in the present study have 45 deg sweep angle as shown in Figure 3-6. They were manufactured by using fine polyamide PA2200

with the rapid prototyping method at the METU BİLTİR Center. The chord length, which was defined as the distance between apex and the trailing edge of the wing, and thickness of all wings were 135 mm and 8 mm, respectively, while the span width, which was defined as the dimension of the trailing edge of the wing, is 270 mm. The leading edges of the wings were beveled on the windward side at an angle of 45 deg. The Base wing does not have any bleeding passages and not shown in the figure. In Figure 3-7, the bleed hole orientations and geometries are represented with a 3-D sketch. The local coordinate system, (x', y'), was used to explain the bleed hole directions. The bleeding holes, which are rectangular in shape, have fixed locations at the pressure side of the wings and are parallel to the leading edge in y' direction. For the geometrical representation of the bleeding holes, r is the width of the holes, l is the length of the holes, d is the distance between the holes and the leading edge and t is the distance between holes. In order to understand the orientation of bleed passages clearly, two angles, β and Φ were defined with respect to local coordinate system. Φ is used for expressing the angle between bleed air direction and x', while β is used for expressing the angle between bleed air direction and y' axis. Φ angle value for all planforms with bleeding is 90 deg, and does not represented in the Figure 3-7 while β angle value changes for three bleeding planforms as $\beta = 13, 18$ and 23 deg, respectively. The back angle, β, of the holes were selected in order to explore the effects of bleeding on the three-dimensional separation over the planform for the attack angles where pre-stall, stall, and post stall regimes, appear on the planform.

In order to perform surface pressure measurements, the wings have pressure taps, which are placed at chordwise distance of $x/C = 0.5$. The Base wing has 20 pressure taps on its suction side, while the others having 13 due to geometrical constraints introduced by bleed holes. The pressure measurement experiments were conducted at the attack angles $\alpha = 13, 16, 17, 18, 19$, and $\alpha = 23$ degrees at Reynolds numbers $Re = 3.5 \times 10^4$, 7.5×10^4 and $Re = 12.5 \times 10^4$, based on the wing chord length, C. For these Reynolds numbers, the free stream velocities were 4.13 $\frac{m}{s}$, 8.86 $\frac{m}{s}$ and 14.76 $\frac{m}{s}$, respectively. The reason of selecting these

angle of attack values is enhancing the possibility of effectiveness of hole with increasing angle of attack, at the pre-stall, stall, and post stall regimes. Especially, it is vital to see the effect of back angles $\beta = 13, 18$ and 23 degrees to the flow field at the similar attack angles, $\alpha = 13, 18$ and 23 degrees, where the free stream directly passes through the holes in parallel orientation.

The near surface flow PIV measurements were conducted at the plane 3 mm ($\Delta z = 3$ mm) away from the surface of the planform, which was the achievable minimum value for the selected angle of attacks considering the entrainment of the tracer smoke particles to the region proximity to the surface of the planform. In order to understand the effect of boundary layer on near surface PIV measurements, $\Delta z = 4$ mm measurements were also conducted where the results are presented in Appendix. The near surface PIV experiments were conducted at the attack angles $\alpha = 17$ and $\alpha = 18$ deg at Reynolds numbers $Re = 3.5 \times 10^4$ and 7.5×10^4. The instantaneous velocity vector patterns are determined by the cross-correlation technique, which compares the locations of particles between identical interrogation areas of two different images with a 50% overlap ratio, satisfying Nyquist criterion. These interrogation areas are in the dimension of 32×32 pixels, with resolution $\Delta/C = 0.024$ for the near surface flow measurements. In Figure 3-8, the overview of experimental setup; i.e., the location of the wing and camera, the planes of laser sheet and free stream, also the plane where pressure measurement taps are located, are demonstrated. In addition, Figures 3-10 and 3-11 represent the experimental matrices for surface pressure measurements and near surface flow PIV, respectively.

3.4 Uncertainty Estimates

During experimentation, experimental data must be considered in terms of uncertainties, which are unavoidable components of the results and required to be measured. In experimental measurements, two types of error are present: systematic and random error. Systematic error can be corrected with the help of calibration. On the other hand, the only way to decrease the random errors is applying uncertainty analysis.

According to Kline and McKlintock [74], the uncertainties created in pressure coefficient, $-C_p$, measurements can be determined by using the method:

$$\omega_R = \left[\left(\omega_{x_1} \frac{\partial R}{\partial x_1} \right)^2 + \left(\omega_{x_2} \frac{\partial R}{\partial x_2} \right)^2 + \cdots + \left(\omega_{x_n} \frac{\partial R}{\partial x_n} \right)^2 \right]^{1/2} \tag{3.3}$$

The above equation is used to calculate the resultant uncertainty, which is shown with ω_p. The pressure scanner measurements have the 0.05 % FS accuracy. The following formula is used for calculating the relative uncertainity:

$$\frac{\omega_R}{R} = u_R \tag{3.4}$$

Recall that the pressure coefficient was calculated via 3.2.

$$C_p = \frac{p - p_\infty}{\frac{1}{2} \rho U_\infty^2} = \frac{p - p_\infty}{p_{dyn}} = \frac{\Delta P}{p_{dyn}}$$

Applying the previously mentioned method may lead to

$$\omega_{C_p} = \left[\left(\omega_p \frac{\partial C_p}{\partial \Delta P} \right)^2 + \left(\omega_p \frac{\partial C_p}{\partial p_{dyn}} \right)^2 \right]^{1/2} \tag{3.5}$$

The differentiation results in :

$$\omega_{C_p} = \left[\left(\frac{\omega_p}{p_{dyn}} \right)^2 + \left(\frac{\omega_p \Delta P}{p_{dyn}^2} \right)^2 \right]^{1/2} \tag{3.6}$$

The calculated results are represented in Table 1. The relative uncertainty value is found as 6.53 % for the minimum absolute $-C_p$ value and the maximum values are supplied in below table.

Table 1 Uncertainty values for the pressure measurements for passive bleed experiments for all planforms at the maximum and the minimum Reynolds numbers for attack angles $\alpha = 13, 16, 17, 18, 19$ and 23 deg.

Uncertainty (%)		Base	$\beta = 13°$	$\beta = 18°$	$\beta = 23°$
α=13 deg	Re=35000	2.19	2.13	2.2	2.12
	Re=125000	0.15	0.15	0.15	0.15
α=16 deg	Re=35000	2.31	2.28	2.28	2.2
	Re=125000	0.17	0.16	0.16	0.16
α=17 deg	Re=35000	2.45	2.4	2.37	2.42
	Re=125000	0.18	0.17	0.16	0.16
α=18 deg	Re=35000	2.58	2.45	2.46	2.43
	Re=125000	0.19	0.19	0.19	0.18
α=19 deg	Re=35000	2.63	2.54	2.46	2.57
	Re=125000	0.2	0.2	0.19	0.19
α=23 deg	Re=35000	3.03	2.81	2.64	2.77
	Re=125000	0.22	0.21	0.2	0.19

The uncertainty values for PIV measurements are determined with the help of commercial software TSI Insight4G. The software utilizes the Peak Ratio (PR) uncertainty method, in which peak to noise peak ratio (PPR) is used to determine uncertainty. The PR method is composed of many possible error sources, including density of seeding particles, pixel displacement and pre-processing of the images. Insight software calculates the uncertainty of each velocity components of the two dimensional velocity vectors, like ΔV_x and ΔV_y, for the PIV application, at some confidence level, and for each Reynolds numbers and planforms, uncertainty values are represented in Table 2. In Figure 3-12, the graphical representation of uncertainty is illustrated, where $\vec{V}$ represents the

velocity vector and ΔV represents the uncertainty value. The circular region shows the area where the tip of the velocity arrow could possibly exist.

Table 2 Uncertainty values for the near surface flow PIV measurements for passive bleed experiments for all planforms at the maximum and minimum Reynolds numbers for attack angles $\alpha = 17$ and 18 deg.

Uncertainty (%)		Base	$\beta = 13°$	$\beta = 18°$	$\beta = 23°$
α=17 deg	Re=35000 (4.13m/s)	5.95	5.86	5.93	5.95
	Re=75000 (8.86 m/s)	6.46	6.84	6.89	3.47
α=18 deg	Re=35000 (4.13 m/s)	5.98	5.87	5.87	5.99
	Re=75000 (8.86 m/s)	7.82	6.86	3.17	3.51

Figure 3-1 View from wind tunnel facility (top) and test section (bottom).
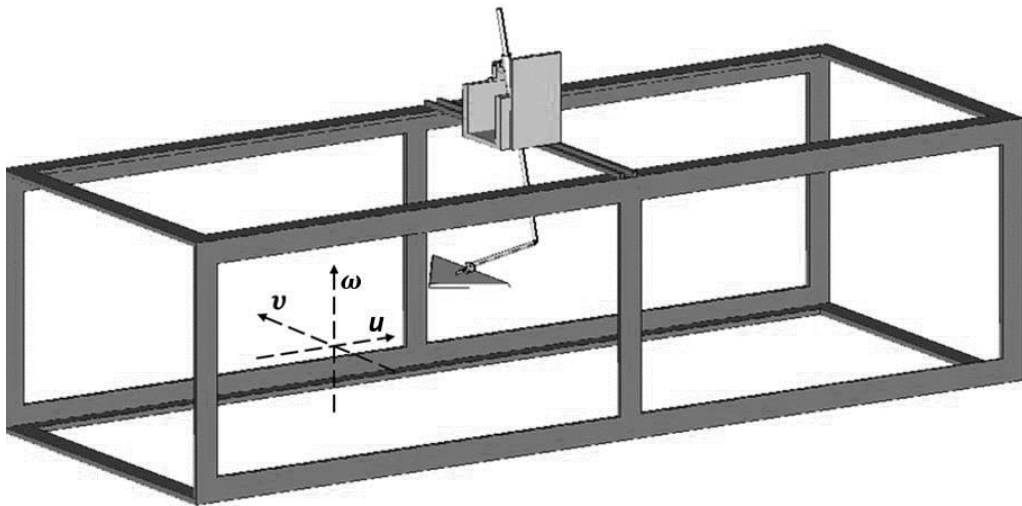
Figure 3-2 Wing model, mount and test section assembly.
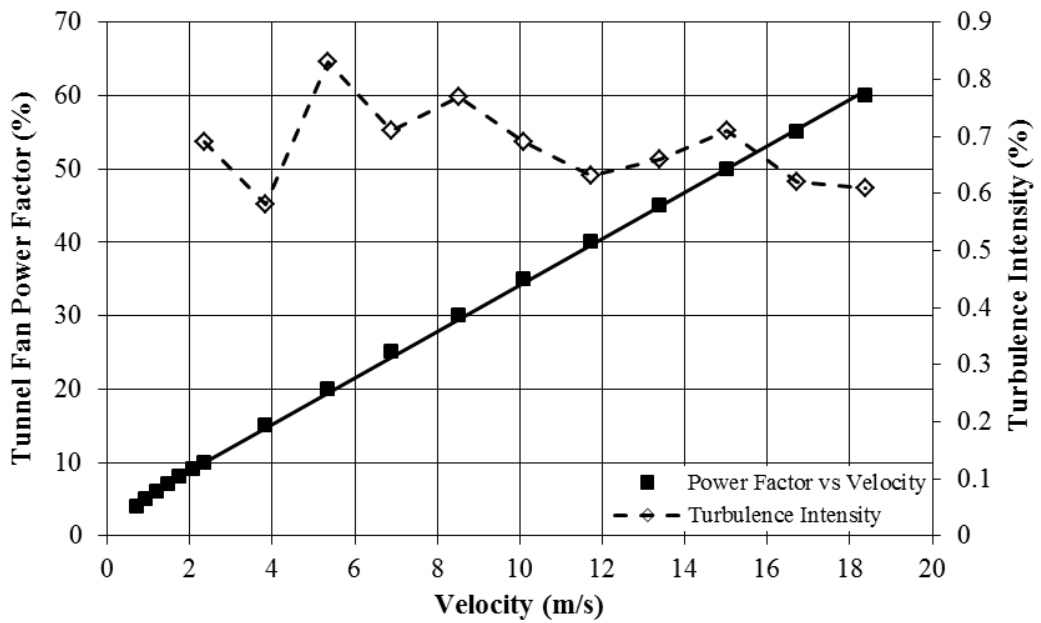
Figure 3-3 Wind tunnel calibration graph.
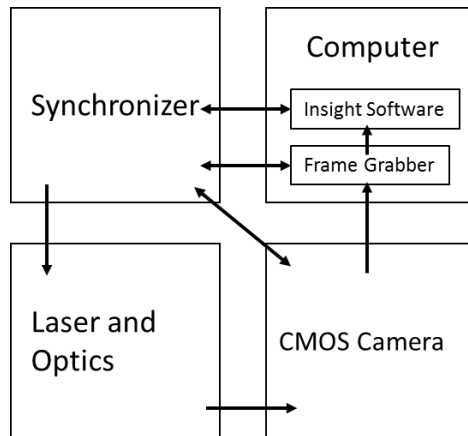
Figure 3-4 Data transfer routes of a 2D PIV system.
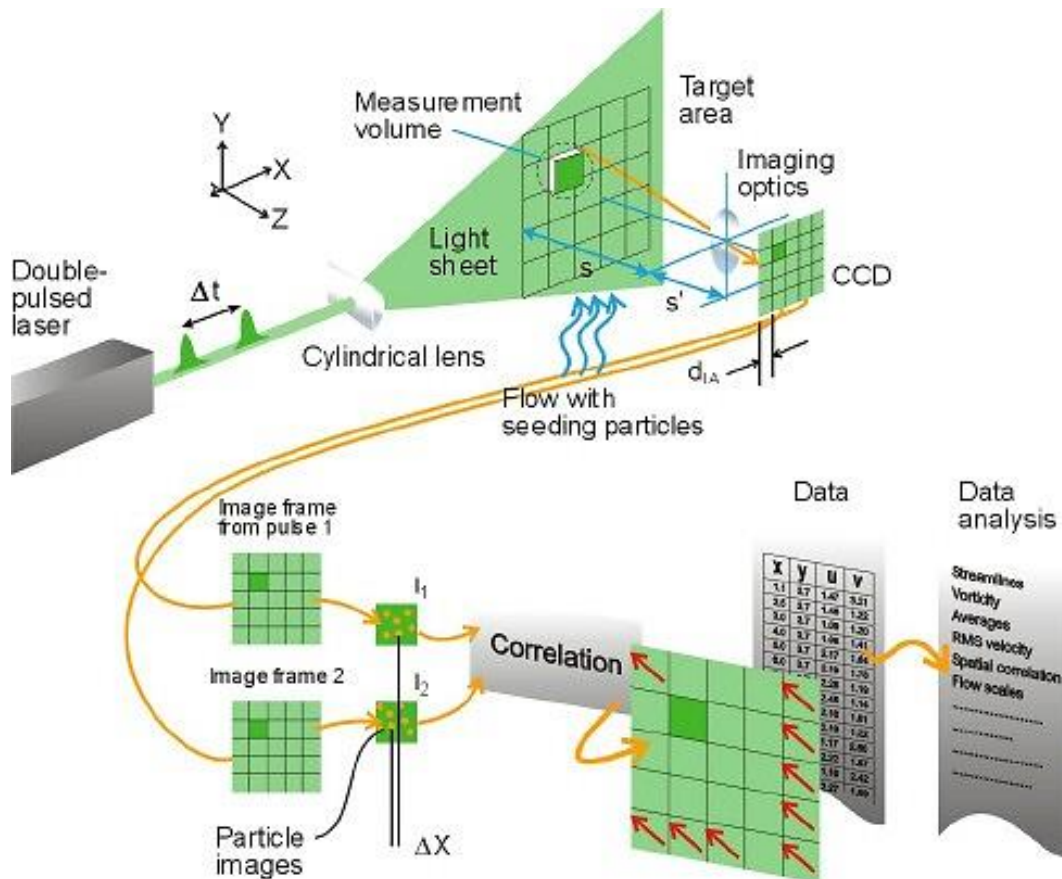
Figure 3-5 Comparison of FFT correlator with Hart correlator on results at 16x16 and 32x32 interrogation windows via streamlines, velocity vectors and non-dimensional axial vorticity contours from top to bottom respectively [83].
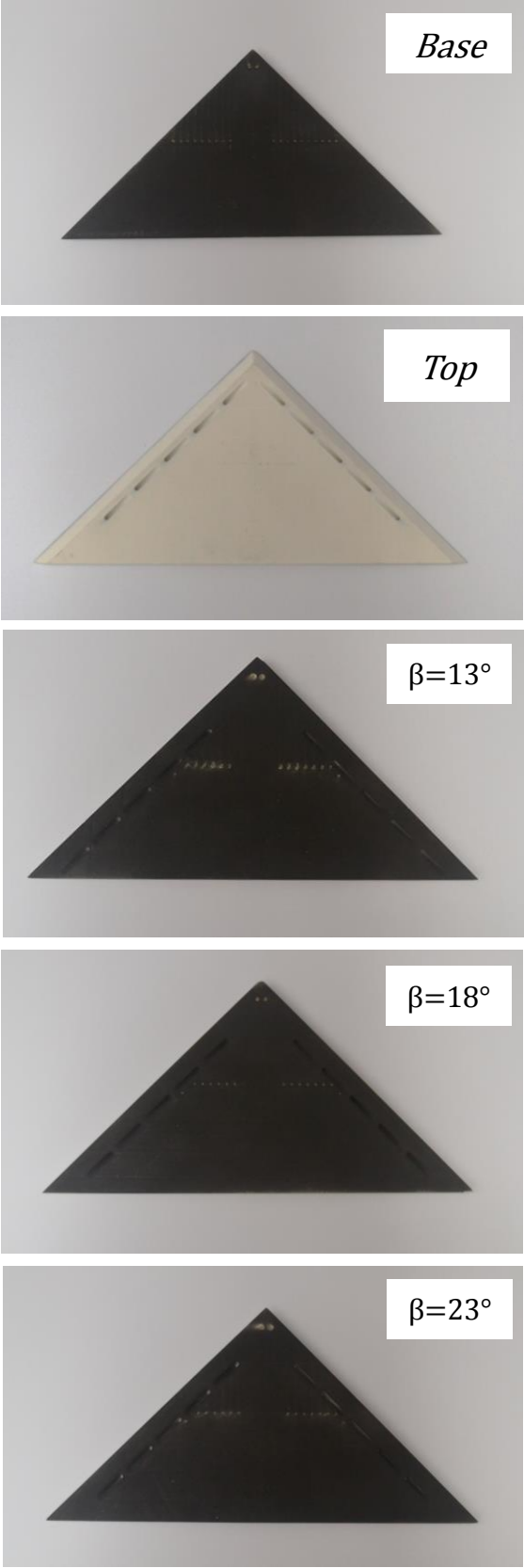
Figure 3-6 Manufactured wings for passive bleed experiments
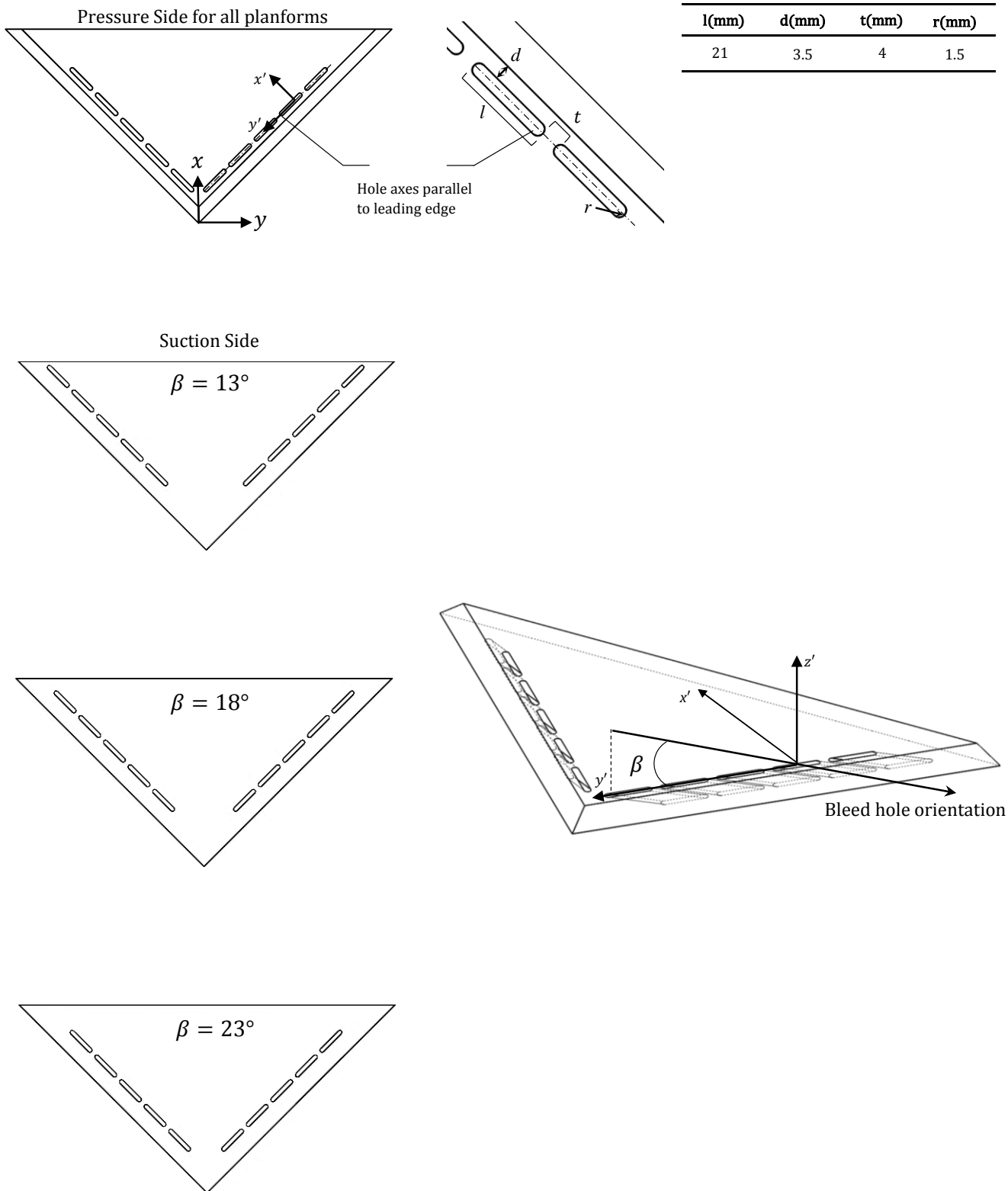
Figure 3-7 Details of bleeding configurations for planforms with back angles, $\beta = 13°, 18°$ and $23°$.

SIDE VIEW

PLAN
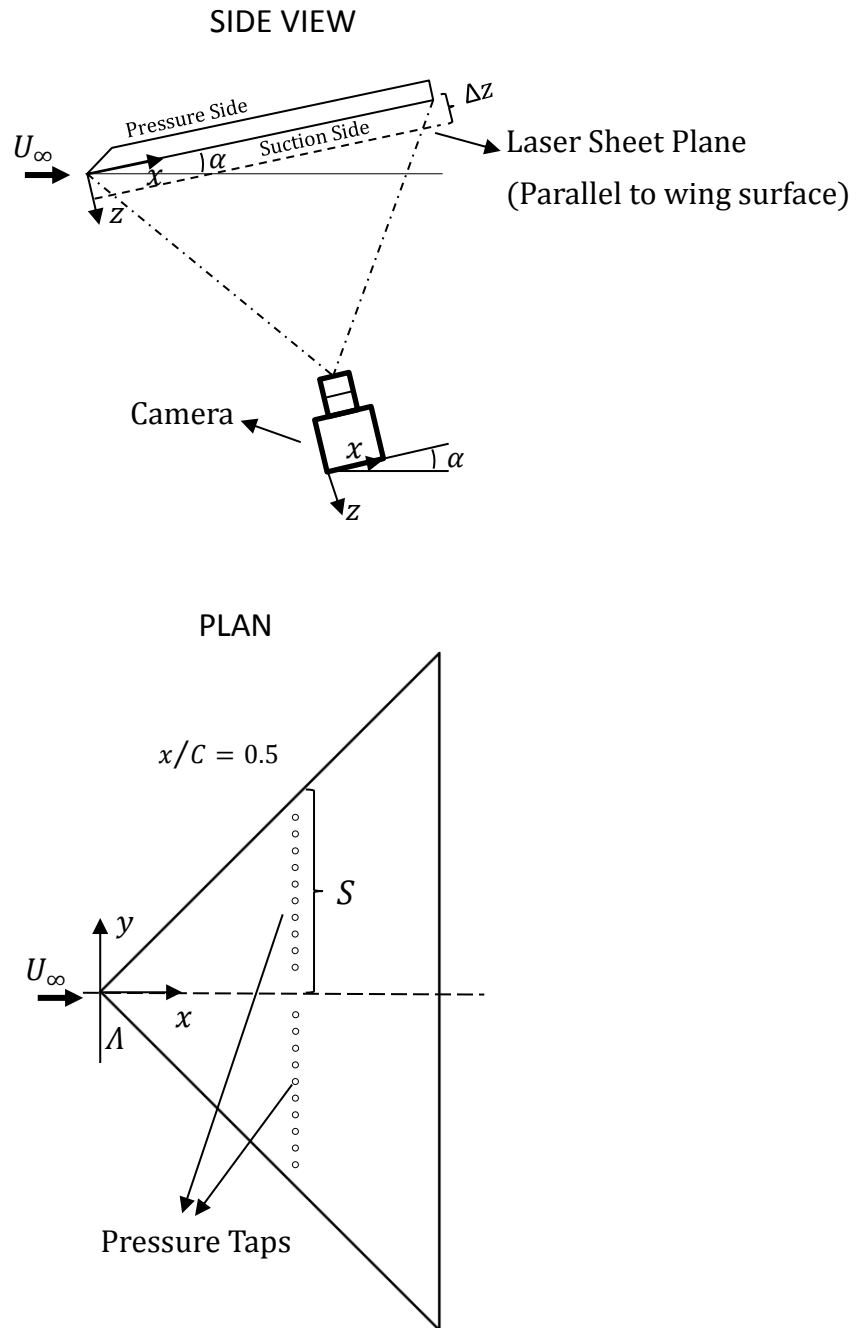
Figure 3-8 Schematic representation of the surface flow PIV and surface pressure
measurement experiment set-up

Highest Suction

Reattachment Location

Symmetry Plane

-Cp

Suction Surface

y/S
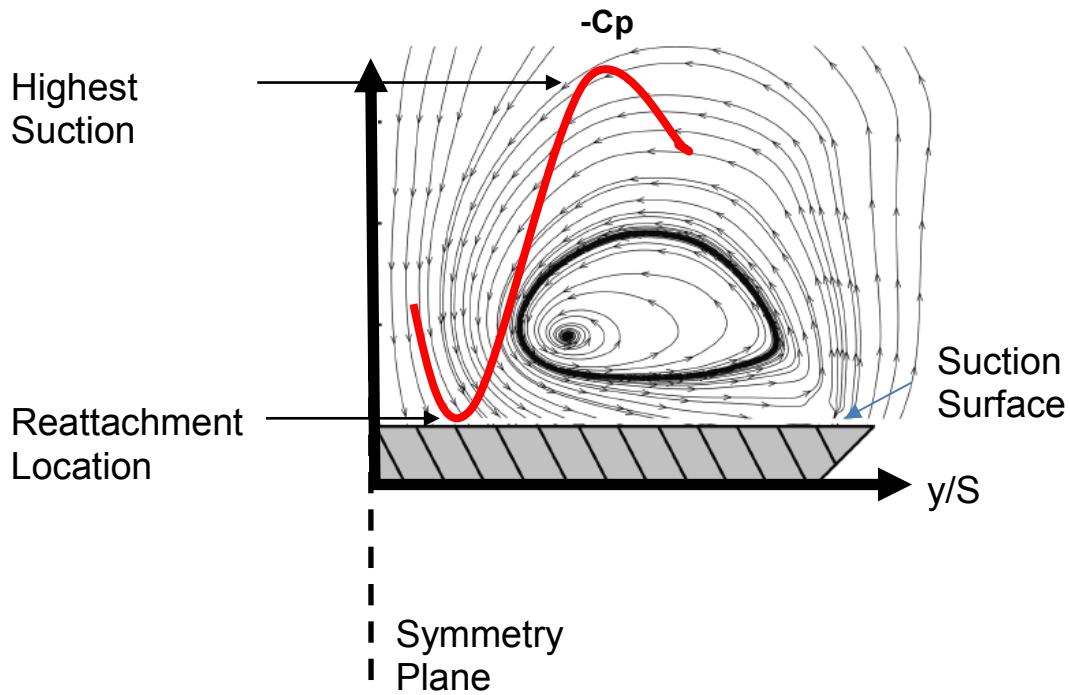
Figure 3-9 $-C_p$ versus y/S representation for a typical leading edge vortex.
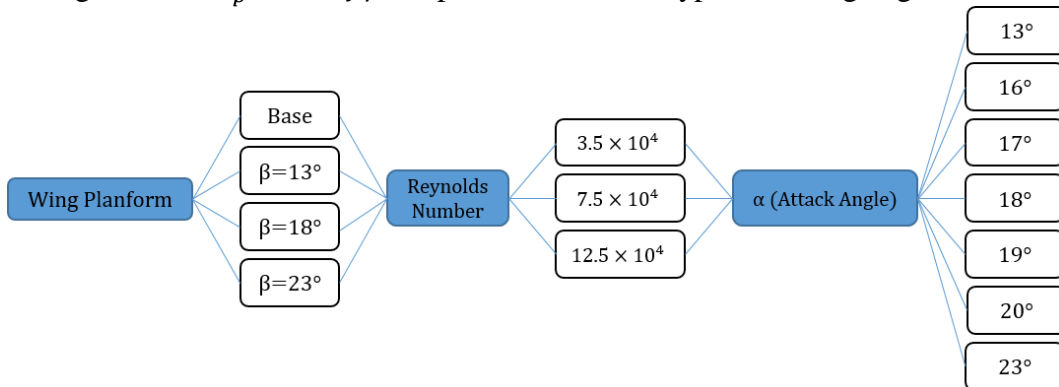
Figure 3-10 Experiment matrix for surface pressure measurements.
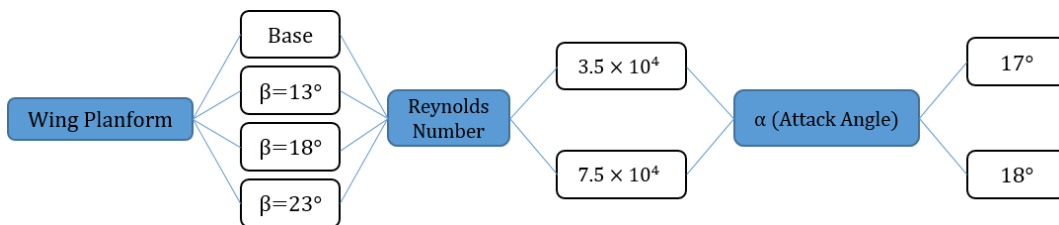
Figure 3-11 Experiment matrix for PIV measurements.
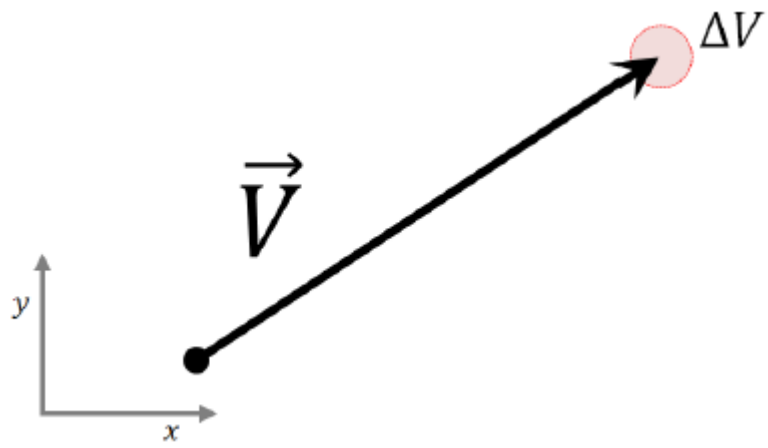
Figure 3-12 A representation of PIV uncertainty, which is shown as circular region [84].

CHAPTER 4

EFFECT OF PASSIVE BLEED ON FLOW STRUCTURE OVER A NONSLENDER DELTA WING

In this chapter, the effect of passive bleeding on flow structure of a 45deg swept non-slender delta wing is discussed in detail. Three different bleeding configurations, back angle values of $\beta = 13, 18$ and 23 deg, were studied to understand whether the control method is effective compared to base planform. A broad range of attack angles varying from $13 < \alpha < 23$ at Reynolds numbers $Re = 3.5 \times 10^4$, 7.5×10^4 and 12.5×10^4 were tested using surface pressure measurement and near surface particle image velocimetry (PIV).

4.1 The Effect of Bleeding on Surface Pressure Measurements

The results of surface pressure measurements in terms of dimensionless pressure coefficient $-C_p$ at chordwise distance $x/C = 0.5$ for all planforms at three Reynolds numbers $Re = 3.5 \times 10^4$, $Re = 7.5 \times 10^4$ and $Re = 12.5 \times 10^4$ are presented in Figures 4-1, 4-2 and 4-3, respectively. The figures are constructed in the same way such that each chart represents $-C_p$ distributions for all planforms including Base, $\beta = 13, 18$, and 23 degrees at single angle of attack. The charts corresponding to six different angles of attack, varying from 13 degree to 23 degree, are positioned in ascending order from top left chart to bottom right chart. Non-dimensional spanwise distance, y/S, measured from symmetry line of the wing corresponds to the horizontal axis, while the vertical axis substitutes for the $-C_p$ values. It is important to note that, as can be seen from the Figure 3-9, the highest $-C_p$ values represent the highest suction locations, while the lowest $-C_p$ values occur at the areas where the flow reattachment to the wing surface takes place.

In Figure 4-1, the results for the Reynolds number $Re = 3.5 \times 10^4$ are presented. The $-C_p$ distributions of all planforms at the attack angles $\alpha = 13$deg represented in the top chart of the left column possess the characteristics of typical leading edge vortex structure, having hump-like pattern with highest and lowest points, expressing suction and reattachment locations. For all bleeding planforms, there is a decrease in the highest $-C_p$ value, indicating a drop in suction, and the corresponding locations gets closer to the wing symmetry line. A similar behavior is also observed for the lowest $-C_p$ values and their locations. The highest deviation for that angle of attack in $-C_p$ values from the Base wing is obtained by planform with back angle $\beta = 18$ deg, which has a 10 % difference between peak points, and the distributions of $-C_p$ values nearly similar for other bleeding planforms ($\beta = 13, 23$ deg). These observations are well in line with the conclusions of Celik et al. [9], reporting that the bleeding decreases the magnitudes of suction pressure coefficient $-Cp$, meaning that it causes a reduction in suction performance of the wing at relatively low incidences. For the results of all planforms at the attack angles $\alpha = 16$ deg and $\alpha = 17$ deg, Base planform starts to indicate separated flow characteristics as can be understood from nearly flat-like $-C_p$ distribution. On the other hand, the wings with bleeding passages exhibit the footprints of vortical structures and flow reattachment to the planform surface. For $\alpha = 17$ deg, the planforms with back angles $\beta = 18$ deg and $\beta = 23$ deg show the best improvement in energizing the flow to obtain vortical structures. Considering the $-C_p$ distributions for $\alpha = 18$ deg, Base, $\beta = 13$ deg, and $\beta = 18$ deg planforms have a flat-like distribution, denoting three-dimensional surface separation, but planform with back angle $\beta = 23$ deg still has a hump-like $-C_p$ distribution, which represents the characteristics of vortical structures and flow reattachment to the planform surface. Considering the angles of attack $\alpha = 19$ and $\alpha = 23$ degrees, none of the planforms demonstrates any significant improvement in $-C_p$ distribution in terms of transforming flat distribution, indicating three dimensional surface separation, to a distribution representing vortical structure.

50

The surface pressure distributions of all planforms for $Re = 7.5 \times 10^4$ and $Re = 12.5 \times 10^4$ are shown in Figures 4-2 and 4-3, respectively. Considering both figures, for all planforms and the corresponding cases, the $-C_p$ distributions exhibit reasonably similar trends with that of $Re = 3.5 \times 10^4$. Particularly, aforementioned discussions regarding the effect of bleeding and its back angle on flat dimensionless pressure coefficients are also evident at Reynolds numbers of $Re = 7.5 \times 10^4$ and $Re = 12.5 \times 10^4$. Considering the cases where the vortical patterns dominate the flow structure, increasing Reynolds number causes a shift in vortical structures, which includes the suction peak and reattachment areas, through the outboard of symmetry line. In addition, the highest $-C_p$ value increases while the lowest $-C_p$ value decreases with increasing Reynolds number, denoting stronger suction and reattachment on the planform surface, which in turn indicates increase in the strength of leading edge vortex. In line with the results of previous Reynolds numbers, planforms having back angles $\beta = 18$ deg and $\beta = 23$ deg exhibit an improvement at attack angle $\alpha = 17$ deg, whereas planform with back angle $\beta = 23$ deg is the only wing that can sustain its efficiency even at attack angle $\alpha = 18$ deg. Thus, it can be concluded that the separated flow structure can be eliminated with the bleeding configuration of the planforms having back angle $\beta = 18$ deg and $\beta = 23$ deg, while it does not a significant effect on the Base and $\beta = 13$ deg back angled planforms.

4.2 The Effect of Bleeding on Flow Structure at $Re = 3.5 \times 10^4$

Based on the results of surface pressure measurements, two angles of attack $\alpha = 17$ and 18 degrees were selected for flow field characterizations. Near surface flow PIV results of bleeding experiments at $Re = 3.5 \times 10^4$ are demonstrated in Figures 4-4 and 4-5, for angles of attack $\alpha = 17$ and 18 degrees, respectively. The approach is similar for all figures: in each row, the time-averaged velocity vectors $< V >$, the time-averaged streamline patterns $< \Psi >$, and the contours of constant non-dimensional vorticity patterns $< \omega_z C/U >$ are represented for the half planforms including the Base and bleeding with back angles $\beta = 13, 18$ and 23 deg from top to bottom, respectively. The contours of constant non-

51

dimensional vorticity $< \omega_z C/U >$ are presented as solid (dark) and dashed (light) lines, designating positive and negative contours, respectively, where positive orientation stands for the vorticity in the direction of the outward normal. For all cases where the constant contours of non-dimensional vorticity in the normal direction are demonstrated, the absolute minimum and incremental values are set as 54 and 3, respectively. ($[|(\omega_z C/U)|]_{min} = 54$ and $[|\Delta(\omega_z C/U)|] = 3$).

In Figure 4-4, the near surface flow PIV results for $\alpha = 17$ deg for $Re = 3.5 \times 10^4$ are represented. According to the patterns of time-averaged streamline, velocity vectors, and vorticity contours, bleeding creates relatively complex flow structures. In Figure 4-4, considering the time-averaged streamline patterns $< \Psi >$, a large-scale focus is observed for Base planform. In literature, this structure has been reported as the result of different experimental studies [66-73]. The existence of a large-scale, inward-swirling surface streamline pattern, which eventuates in a stable focus is an indicator of three-dimensional surface separation [45]. For all planforms, the magnitudes of time-averaged velocity vectors $< V >$ abruptly decrease at the downstream of the leading edge; especially, the magnitude of the velocity vectors $< V >$ is very small inside the central area of the large swirling patterns and near the symmetry line of planform B. Furthermore, the vorticity concentrations at previously defined minimum levels are not apparent and the magnitude of velocity vectors near the symmetry line of the planform are very small for the Base planform, which are the other indications of separated flow without any strong reattachment.

It is interesting to observe that, for the planforms with bleeding, the focus of this large-scale swirl move through the apex of the wing, compared to Base planform. In addition, the spatial extend of the area governed by very small velocities decreases while the magnitude of the $< V >$ near the symmetry plane shows an increase in planforms with bleeding with regard to the Base planform, indicating the strength of reattachment is apparently increased. Considering the contours of constant non-dimensional vorticity patterns $< \omega_z C/U >$, a significant negative structure of $< \omega_z C/U >$ is present along the leading edge of all planforms, which is an apparent representation of the three-dimensional shear layer instability. For Base planform, the vorticity concentrations at previously defined minimum levels

52

are not apparent because of the separated flow. In all planforms with back angles, the vorticity patterns are much more elongated compared to Base planform, leading a significant increase in the surface vorticity concentrations are observed. Approximately 150 % increase in the maximum levels of the constant vorticity contours are observed in planform with back angle $\beta = 18$ deg, whereas 100 % and 66 % improvements is obtained for the planform with back angle $\beta = 23$ and $\beta = 13$ deg, respectively. The results demonstrate that for this attack angle and Reynolds number, all planforms with back angles might ensure the recovery of vortical structure on the wing surface, which is also confirmed by the results of surface pressure measurements.

The corresponding flow structures for the attack angle $\alpha = 18$ deg are represented in Figure 4-5. The results are consistent with the flow patterns of previous attack angle and surface pressure measurements. Base planform has a large-scale swirling structure, of which focus has small magnitudes of velocity vectors. Actually, the magnitude of velocity vectors abruptly decreases at the downstream of the leading edge, which are also small for the area near the symmetry line of planform B. The reattachment is shifted towards the outboard of the symmetry line and the strength of the reattachment is increased in all bleeding planforms, as can be seen from the increased values of the velocity vectors close to the wing center. According to the time-averaged streamline patterns $< \Psi >$, a shift in the focus of large-scale swirling structure towards the apex of the wing is observed for all bleeding planforms. These results are supported by the constant vorticity concentrations, which demonstrate an increase in constant non-dimensional vorticity contours $< \omega_z C / U >$ for all bleeding planforms, compared to Base wing, having a totally deteriorated vorticity patterns. However, for this case, the most apparent improvement is observed for the planform with back angle $\beta = 23$ deg, which has the highest magnitude of the velocity vectors and the vorticity contours, meaning stronger reattachment and recovery of vortical structures, as expected from the surface pressure measurement results. Approximately 66 % increase in the maximum levels of the constant vorticity contours are obtained in planform with back angle $\beta = 18$ and 23 deg.

4.3 The Effect of Bleeding on Flow Structure at $Re = 7.5 \times 10^4$

As explained in previous section for $Re = 3.5 \times 10^4$, the same approach was used in figure constructions in this section. In Figure 4-6, the near surface flow PIV results for $\alpha = 17$ deg for $Re = 7.5 \times 10^4$ are represented. As can be seen from the patterns of time-averaged streamline, velocity vectors, and vorticity contours, bleeding creates relatively complex flow structures. The flow structure on Base planform represents the properties of separated flow; i.e., a large-scale swirl structure with a focus located at the middle portion of the wing is observed with very small magnitudes of velocity vectors and vorticity concentrations throughout the planform. However, for the other planforms with bleeding, flow structure shows the footprints of the recovery of the vortical structures because the focus of the large-scale pattern shifts through the apex of planform in all bleeding configurations, and the reattachment becomes stronger according to the magnitudes of the velocity vectors $< V >$ at the areas near to the symmetry line. In addition, the constant contours of the non-dimensional vorticity magnitudes $< \omega_z C/U >$ represent an elongated layer of vorticity, and vorticity concentrations apparently increase in all bleeding planforms. Compared to the Base planform, 25 %, 75 % and 50 % increases are achieved in maximum levels of vorticity concentrations for the bleeding planforms with back angles $\beta = 13, 18$ and 23 deg, respectively. According to the strength of reattachment and the magnitude of the constant vorticity contours, the highest improvement is obtained for the back angle $\beta = 18$ and 23 deg, which is consistent with surface pressure measurements.

The corresponding flow structures for the attack angle $\alpha = 18$ deg are represented in Figure 4-7. The results are consistent with the flow patterns of previous attack angle and Reynolds number. The time-averaged streamline patterns $< \Psi >$, shifting in the focus of large-scale swirling structure towards the apex of the wing is observed, herein a stronger suction and reattachment are also present according to the time-averaged velocity vectors $< V >$. The most important point to highlight is the bleeding planform with back angle $\beta = 23$ deg represents the highest increase of the contours of constant non-dimensional

54

vorticity patterns $< \omega_z C/U >$ compared to Base planform. Approximately 100 % percent increase in maximum level of constant contours of non-dimensional vorticity is obtained, as expected from the results of surface pressure measurement. The results support the idea that vortical structure might be recovered with proper bleeding configuration at three-dimensional surface separation/stall regime.

In the current study, the effects of passive bleeding with back angles $\beta = 13, 18$ and 23 deg have been explored. For this object, surface pressure measurements and Particle Image Velocimetry techniques were utilized in a low speed wind tunnel for Reynolds numbers $Re = 3.5 \times 10^4$, 7.5×10^4 and 12.5×10^4 at attack angles $13 < \alpha < 23$ using four 45 deg sweep delta wings, with one Base and three bleeding planforms. According to the results of these studies, it observed that bleeding alters the overall flow field over a non-slender delta wing. At sufficiently high incidences, where three-dimensional separation takes place, proper implementation of bleeding might recover the vortical structures, whereas at relatively low angle of attack values, bleeding causes a reduction in suction performance of the wing. It might be concluded that with the proper bleeding configuration, three-dimensional surface separation from the surface can be eliminated and flow field over the 45 deg sweep delta wings can be improved.
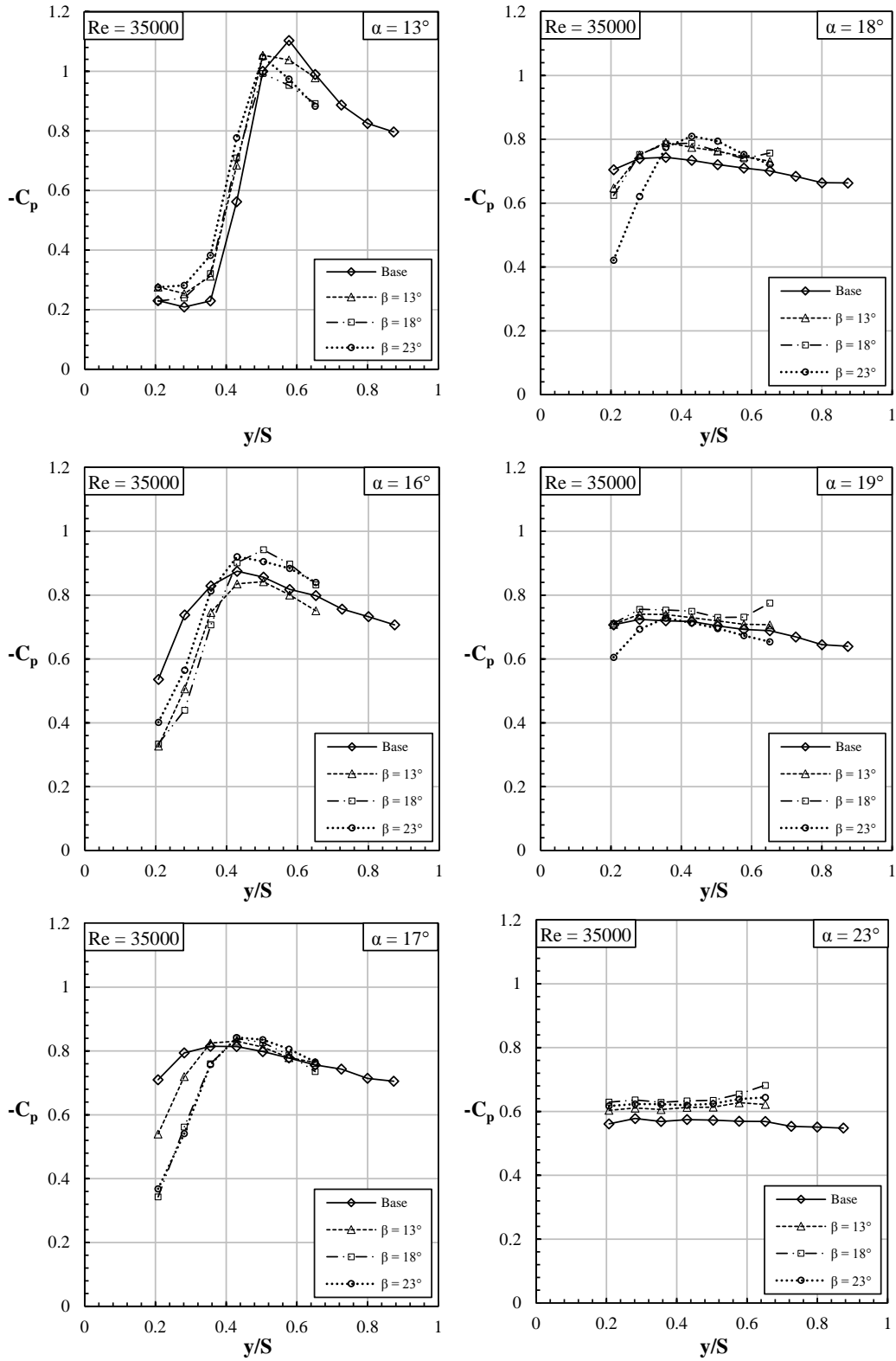
Figure 4-1 $-C_p$ distributions of half span Base, $\beta = 13°$, $\beta = 18°$ and $\beta = 23°$ planforms at angle of attacks $\alpha = 13, 16, 17, 18, 19$ and 23 deg at $Re = 3.5 \times 10^4$.

56
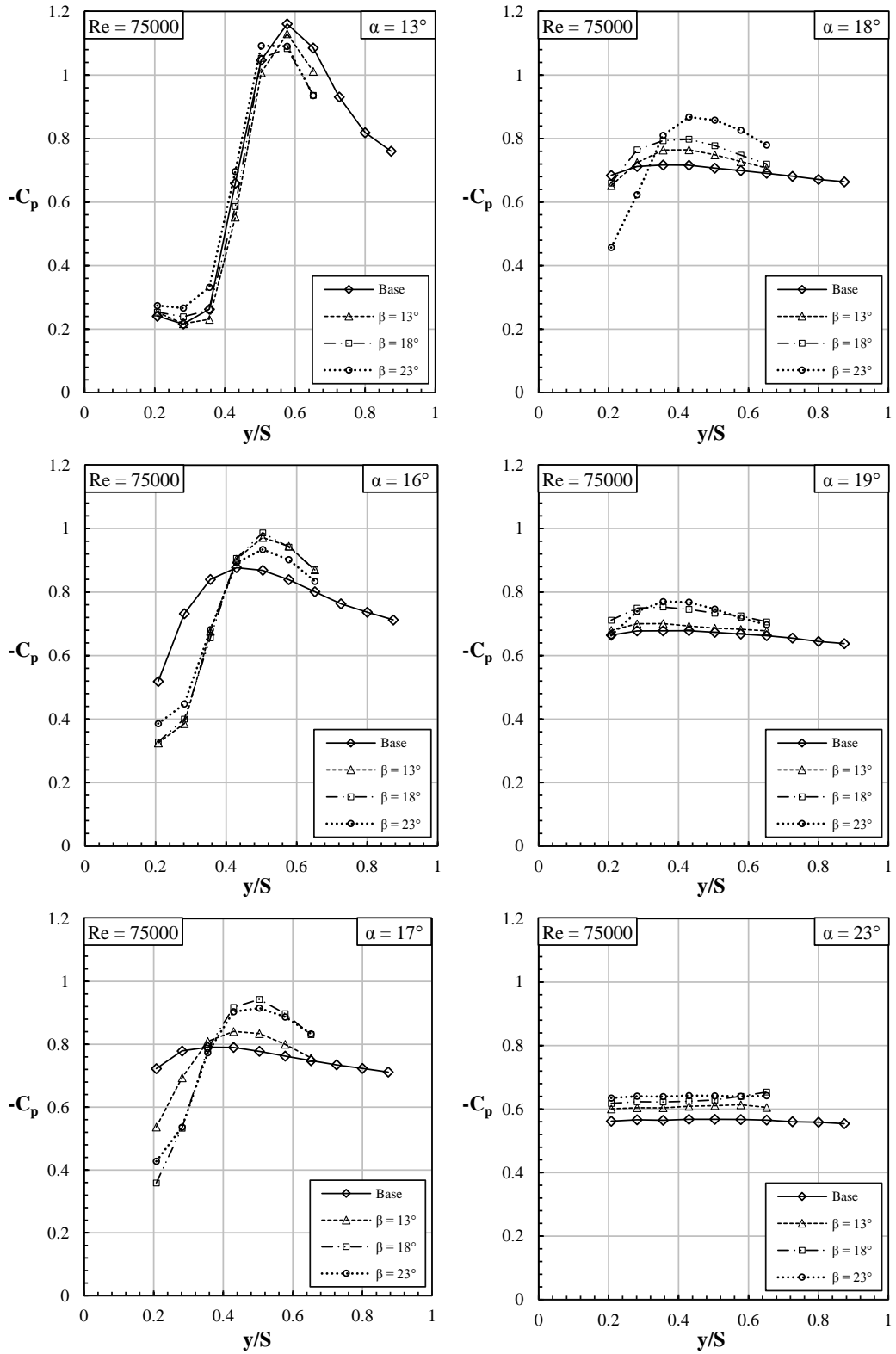
Figure 4-2 $-C_p$ distributions of half span Base, $\beta = 13°$, $\beta = 18°$ and $\beta = 23°$ planforms at angle of attacks $\alpha = 13, 16, 17, 18, 19$ and 23 deg at $Re = 7.5 \times 10^4$.
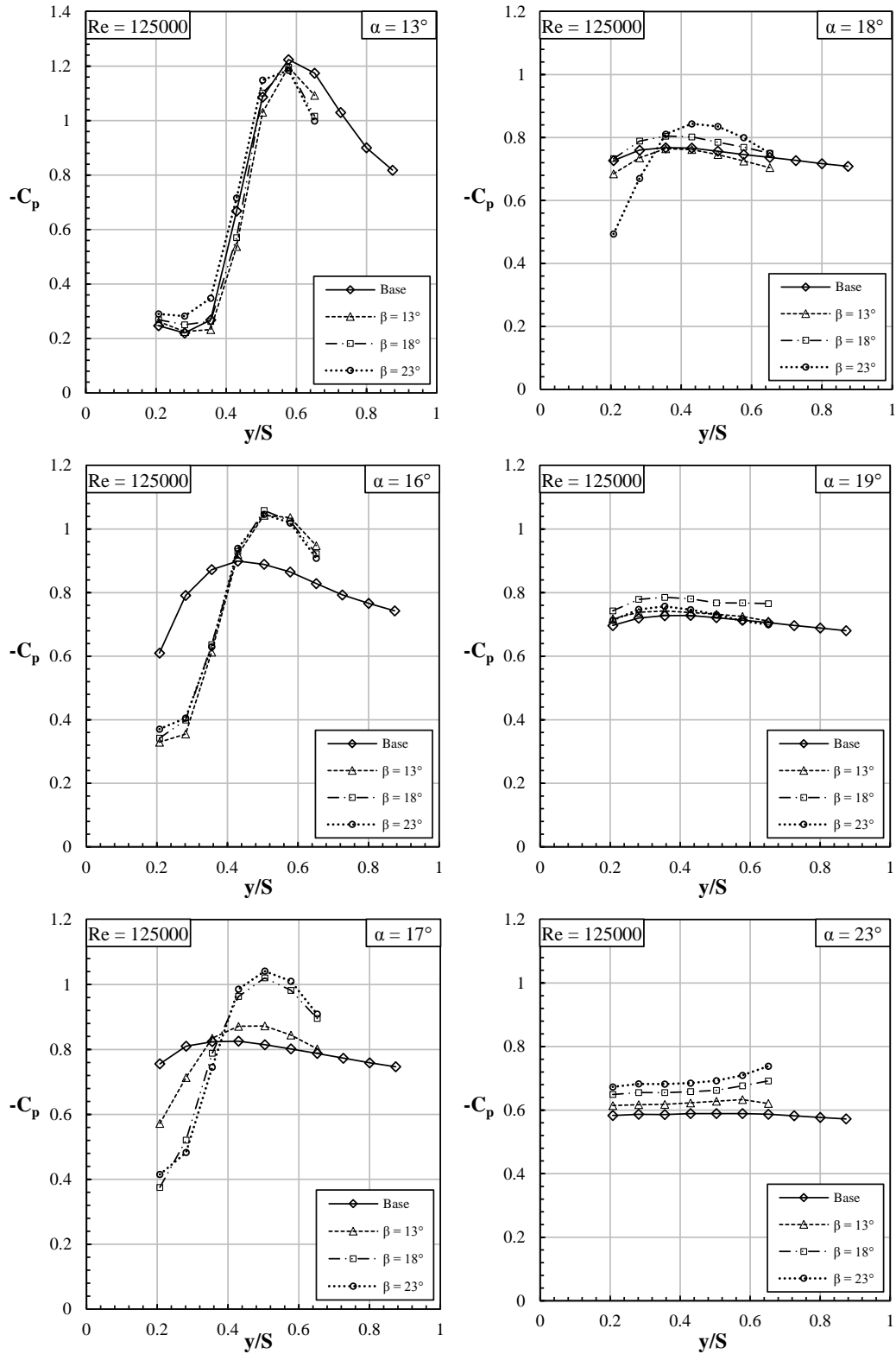
Figure 4-3 $-C_p$ distributions of half span Base, $\beta = 13°$, $\beta = 18°$ and $\beta = 23°$ planforms at angle of attacks $\alpha = 13, 16, 17, 18, 19$ and 23 deg at $Re = 12.5 \times 10^4$.
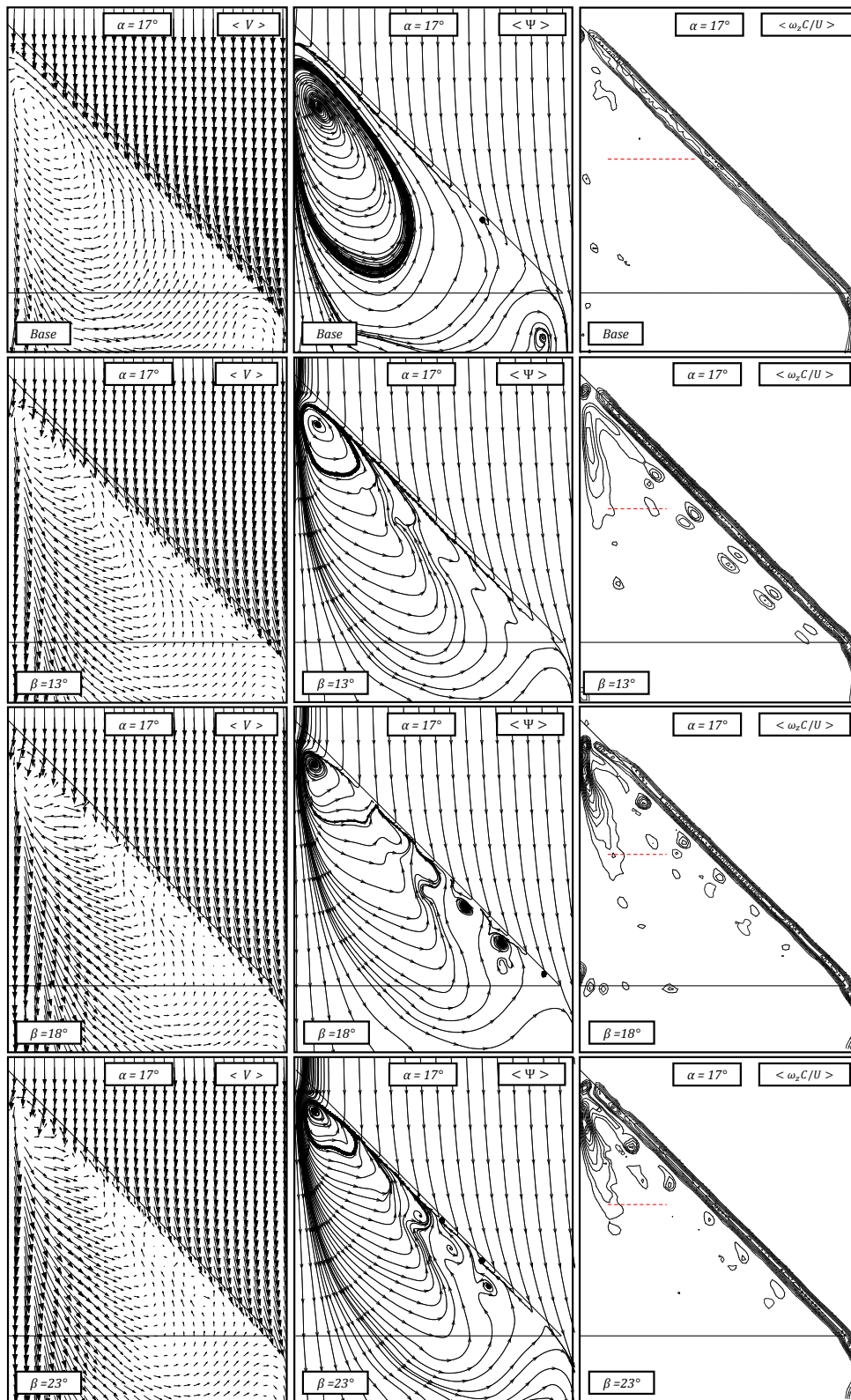
Figure 4-4 Patterns of time-averaged velocity vectors $\langle V \rangle$, streamlines $\langle \Psi \rangle$ and constant contours of non-dimensional vorticity $\langle \omega C/U \rangle$ at angle of attack $\alpha = 17$ deg for $Re = 3.5 \times 10^4$: $[|\langle \omega C/U \rangle|]_{min} = 54$, $\Delta[|\langle \omega C/U \rangle|] = 3$

59
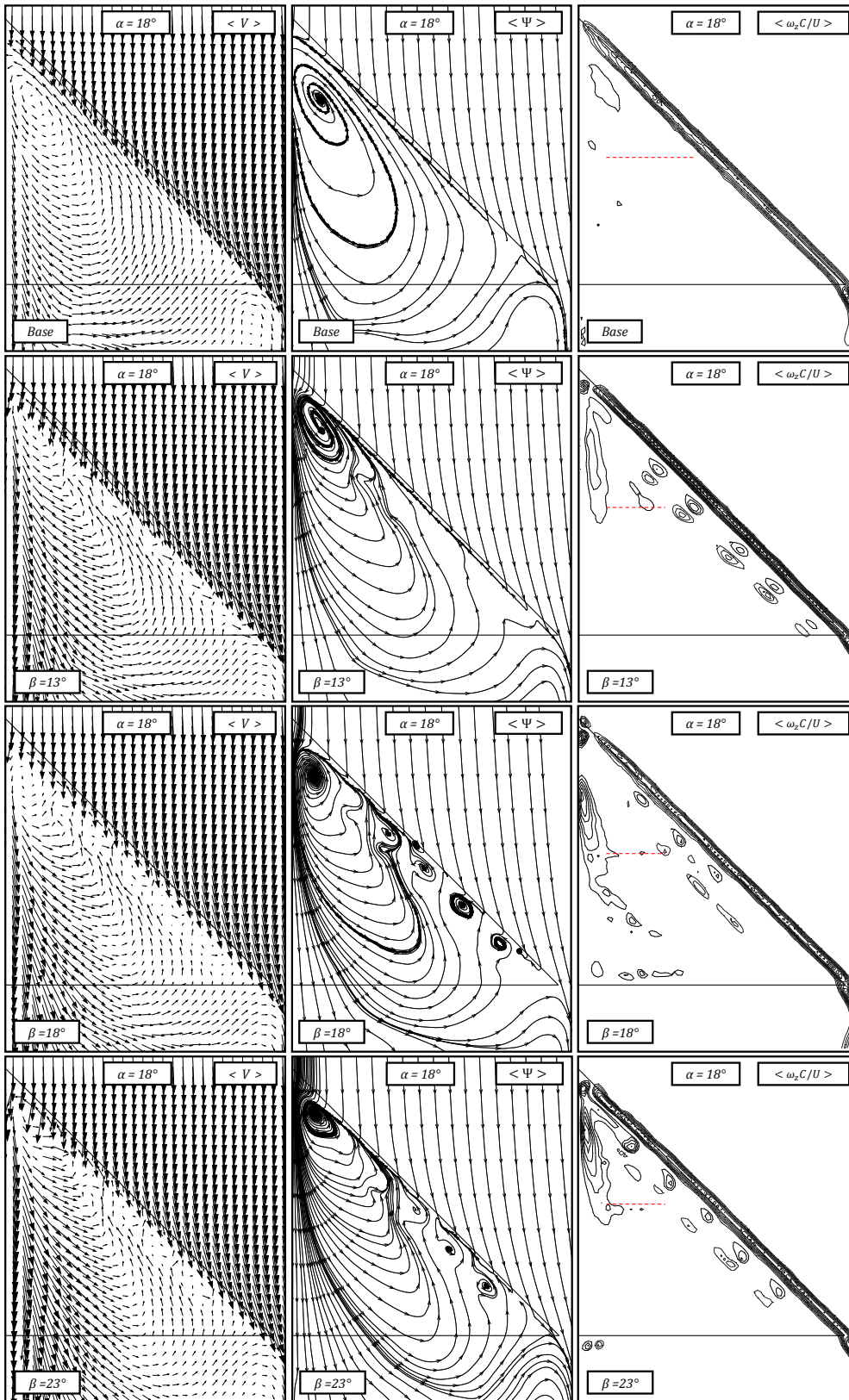
Figure 4-5 Patterns of time-averaged velocity vectors $\langle V \rangle$, streamlines $\langle \Psi \rangle$ and constant contours of non-dimensional vorticity $\langle \omega_z C/U \rangle$ at angle of attack $\alpha = $ 18 deg for $Re = 3.5 \times 10^4$: $[|\langle \omega_z C/U \rangle|]_{min} = 54$, $\Delta[|\langle \omega_z C/U \rangle|] = 3$

60
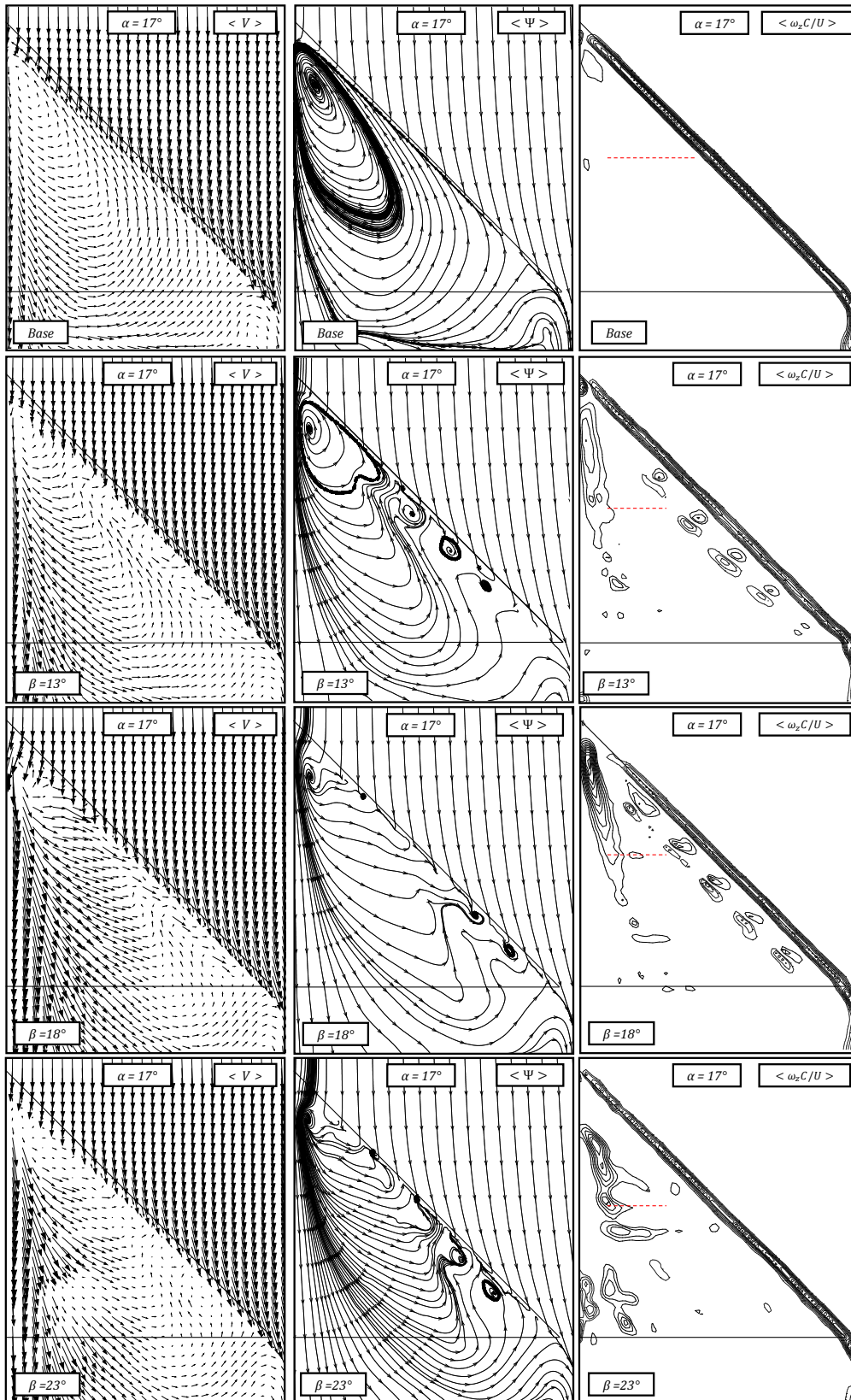
Figure 4-6 Patterns of time-averaged velocity vectors $\langle V \rangle$, streamlines $\langle \Psi \rangle$ and constant contours of non-dimensional vorticity $\langle \omega_z C/U \rangle$ at angle of attack $\alpha = 17$ deg for $Re = 7.5 \times 10^4$: $[|\langle \omega_z C/U \rangle|]_{min} = 54$, $\Delta[|\langle \omega_z C/U \rangle|] = 3$

Figure 4-7 Patterns of time-averaged velocity vectors $\langle V \rangle$, streamlines $\langle \Psi \rangle$ and constant contours of non-dimensional vorticity $\langle \omega_z C/U \rangle$ at angle of attack $\alpha = 18$ deg for $Re = 7.5 \times 10^4$: $[|\langle \omega_z C/U \rangle|]_{min} = 54$, $\Delta[|\langle \omega_z C/U \rangle|] = 3$

CHAPTER 5

CONCLUSION

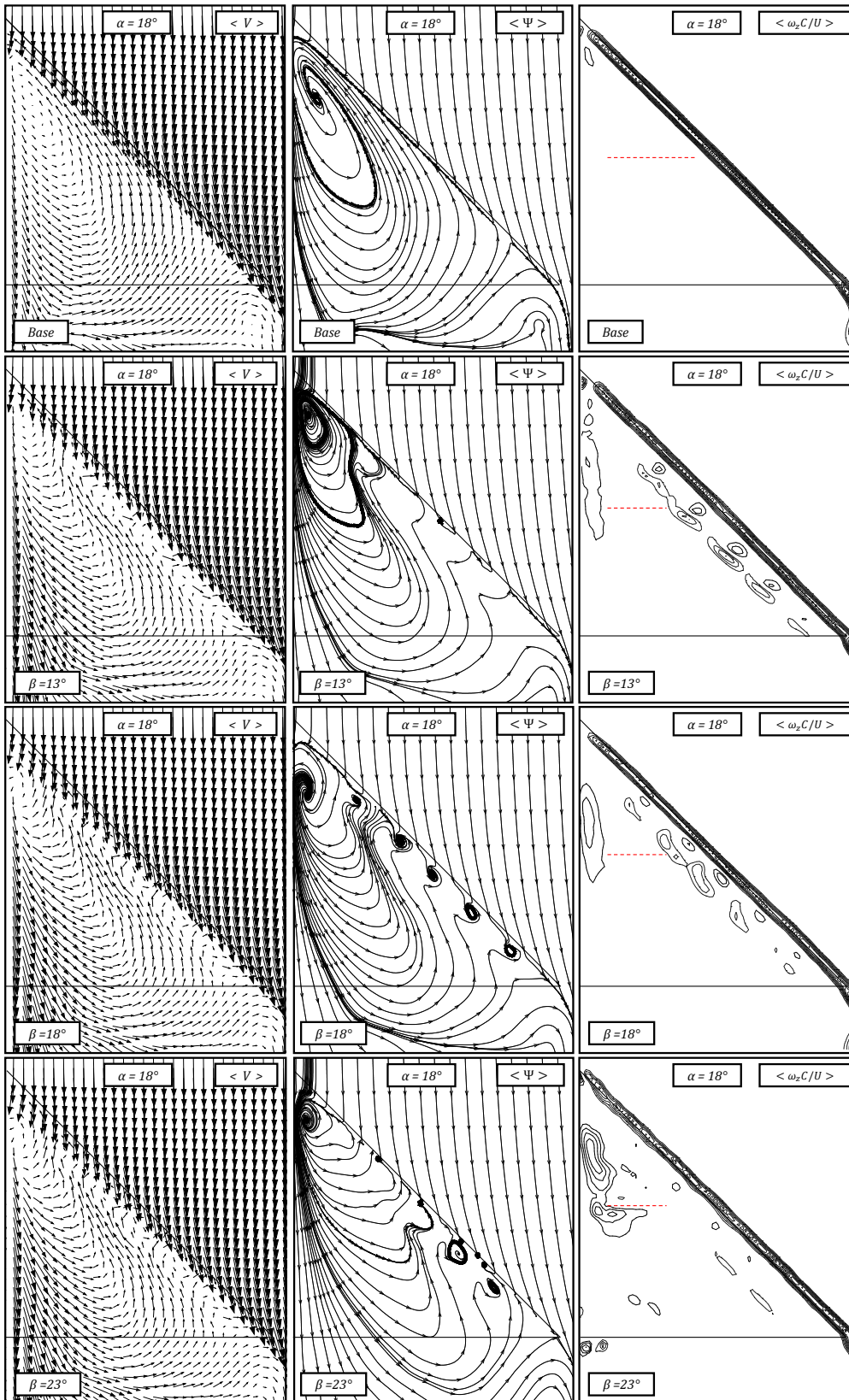The current study is devoted to explore a passive bleeding method to control the flow structure over a 45 deg sweep delta wings in order to improve the pre-to-post stall conditions. Passive bleeding is a flow control method, which is used for directing the high-pressure air from the pressure side to suction side of the planform without any energy input. For this purpose, three non-slender planforms having the holes with different back angles, $\beta = 13, 18$ and 23 deg, respectively through the leading edges were designed and manufactured. In order to understand their effects on flow structure, different quantitative methods were utilized, including surface pressure measurements and Particle Image Velocimetry to a broad range of attack angles $13 < \alpha < 23$ at Reynolds numbers $Re = 3.5 \times 10^4$, 7.5×10^4 and 12.5×10^4. The results of bleeding planforms were compared with the result of the Base planform to observe the improvement.

According to the results and comparisons of the current study, the following general conclusions can be drawn:

- Entire flow field over the planform is changed with the passive bleeding method, and additional swirl structures are created at the hole areas.

- At sufficiently high angle of attack (i.e., $\alpha = 16, 17$ and 18 deg), a recovery of vortical structures with apparent increase in suction pressure coefficient $-C_p$ and maximum level of constant contours of non-dimensional vorticity is observed, whereas the Base planform experiences three-dimensional surface separation for those incidences. The focus of large-scale streamline pattern shifts though the apex of the wing for all back angles. From the near surface flow PIV results, the magnitude of the velocity vectors increase near the symmetry line of all planforms with

63

bleeding, indicating that the reattachment to the planform surface becomes stronger in pre-stall regime. Indeed, the improvements on flow structure are more obvious for the bleeding planforms with back angles $\beta = 18$ and 23 deg, whereas the bleeding planform with back angles $\beta = 13$ deg is not sufficiently effective to recover the vortical structures, as can be clearly seen from the $-C_p$ distributions and maximum level of constant contours of non-dimensional vorticity values. Thus, it might be concluded that elimination of three-dimensional surface separation is accomplished by passive bleeding method with higher back angles ($\beta = 18$ and 23 deg). Especially, the bleeding planform with higher back angle ($\beta = 23$ deg) is much more effective in higher attack angles (i.e., $\alpha = 18$ deg) than smaller back-angled bleeding planforms.

- Contrarily, at relatively low attack angles ($\alpha = 13$ deg, for this experiments), bleeding causes a drop in the magnitude of pressure coefficient $-C_p$ for all back angles. This indicates that for low angles of attack, bleeding creates loss in suction over the planform, which is well in line with the conclusions of Celik et al. [9].

- For much higher angle of attacks $\alpha = 19$ degree and higher which presumably correspond to post stall regime, bleeding is not effective in eliminating the separated flow.

To conclude, according to the results of the present study, the back-angled passive bleeding configuration might effectively be used to prevent the surface separation on a non-slender delta wing with appropriate back angle.

5.1 Recommendations for Future Work

In this study, a passive flow control technique, which is bleeding with different back angles, is proposed and studied in detail. The main motivation of this study was exploring the effect of bleeding with back angle on flow structure over a 45 deg sweep delta wing, and whether it can effectively be used as a control technique. The results indicate that this method has a great potential for further investigations, which are explained below.

- In addition to the characterization of flow structure for passive bleeding, its effects on aerodynamic forces should also be determined. For this purpose, force measurement experiments for all planforms need to be conducted.

- In addition to the effect of back angle, which is investigated in the current study, the effects of passage geometry and locations on flow structure need to be characterized.

- The current and the previous studies about passive bleeding on non-slender delta wings aim to understand the flow structure over a 45 deg sweep delta wing only. The wings with different sweep angles should also be studied to generalize the conclusions of the present study.

REFERENCES

[1]   P. B. Earnshaw and J. a Lawford, "Low-Speed Wind-Tunnel Experiments on a Series of Sharp-Edged Delta Wings," *Aeronautical*, no. 3424, 1964.

[2]   I. Gursul, "Vortex flows on UAVs: Issues and challenges," in *Aeronautical Journal*, 2004, vol. 108, no. 1090, pp. 597–610.

[3]   I. Gursul, Z. Wang, and E. Vardaki, "Review of flow control mechanisms of leading-edge vortices," *Progress in Aerospace Sciences*, vol. 43, no. 7–8. pp. 246–270, 2007.

[4]   I. Gursul, R. Gordnier, and M. Visbal, "Unsteady aerodynamics of nonslender delta wings," *Prog. Aerosp. Sci.*, vol. 41, no. 7, pp. 515–557, 2005.

[5]   M. R. Gordnier, R. E., Visbal, "Compact Difference Scheme Applied to Simulation of Low-Sweep Delta Wing Flow," *AIAA J.*, vol. 43, no. 8, pp. 1744–1752.

[6]   C. Breitsamter, "Unsteady flow phenomena associated with leading-edge vortices," *Progress in Aerospace Sciences*, vol. 44, no. 1. pp. 48–65, 2008.

[7]   I. Gursul, "Review of unsteady vortex flows over slender delta wings," *J. Aircr.*, vol. 42, no. 2, pp. 299–319, 2003.

[8]   G. S. Taylor and I. Gursul, "Buffeting Flows over a Low-Sweep Delta Wing," *AIAA J.*, vol. 42, no. 9, pp. 1737–1745, 2004.

[9]   A. Çelik, C. Çetin, and M. M. Yavuz, "Effect of Passive Bleeding on Flow Structure over a Nonslender Delta Wing," pp. 1–11.

[10]   G. E. Erickson, "Water-Tunnel Studies of Leading-Edge Vortices," *J. Aircr.*, vol. 19, no. 6, pp. 442–448, Jun. 1982.

[11]   E. C. Polhamus, "Predictions of Vortex-Lift Characteristics by a Leading-Edge Suction Analogy," no. 4, pp. 193–199, 1971.

[12]   M. GAD-EL-HAK and R. F. BLACKWELDER, "The discrete vortices from a delta wing," *AIAA J.*, vol. 23, no. 6, pp. 961–962, Jun. 1985.

[13]   G. Taylor, T. Schnorbus, and I. Gursul, "An Investigation of Vortex Flows Over Low Sweep Delta Wings," *AIAA Aerosp. Meet. Exhib.*, no. June, 2003.

[14]   B. Yaniktepe and D. Rockwell, "Flow Structure on a Delta Wing of Low Sweep Angle," *AIAA J.*, vol. 42, no. 3, pp. 513–523, 2004.

[15]   W. Jin-Jun and Z. Wang, "Experimental investigations on leading-edge vortex structures for flow over non-slender delta wings," *Chinese Phys. Lett.*, vol. 25, no. 7, pp. 2550–2553, 2008.

[16]   H. Werlé, "Quelques Résultats Expérimentaux Sur les Ailes en Flèche, aux

Faibles Vitesses, Obtenus en Tunnel Hydrodynamique," *La Rech. Aéronautique*, 1954.

[17] M. V Lowson, "Some Experiments with Vortex Breakdown," *J. R. Aeronaut. Soc.*, vol. 68, no. 641, pp. 343–346, 1964.

[18] P. B. Earnshaw, "An Experimental Investigation of the Structure of a Leading Edge Vortex," no. 3281, p. 11, 1962.

[19] M. Yavuz, M. Elkhoury, and D. Rockwell, "Near-surface Topology and Flow Structure on a Delta Wing," *AIAA J.*, 2004.

[20] A. Çelik and M. M. Yavuz, "Effect of Edge Modifications on Flow Structure of Low Swept Delta Wing," *AIAA J.*, vol. 54, no. 5, pp. 1789–1797, Mar. 2016.

[21] G. Taylor, Z. Wang, E. Vardaki, and I. Gursul, "Lift Enhancement over Flexible Nonslender Delta Wings," *AIAA J.*, vol. 45, no. 12, pp. 2979–2993, 2007.

[22] D. I. Greenwell, "Gurney Flaps on Slender and Nonslender Delta Wings," *J. Aircr.*, vol. 47, no. 2, pp. 675–681, Mar. 2010.

[23] R. C. Nelson and A. Pelletier, "The unsteady aerodynamics of slender wings and aircraft undergoing large amplitude maneuvers," *Prog. Aerosp. Sci.*, vol. 39, no. 2, pp. 185–248, 2003.

[24] I. Gursul, "Origin of Vortex Wandering over Delta Wings," *J. Aircr.*, vol. 37, no. 2, pp. 1996–1998, 1999.

[25] N. G. Verhaagen, "Leading-Edge Radius Effects on Aerodynamic Characteristics of 50-Degree Delta Wings," *J. Aircr.*, vol. 49, no. 2, pp. 521–531, Mar. 2012.

[26] W. Gu, O. Robinson, and D. Rockwell, "Control of Vortices on a Delta Wing by Leading-edge Injection," *AIAA J.*, vol. 31, no. 7, pp. 1177–1186, 1993.

[27] N. J. Wood, L. Roberts, and Z. Celik, "Control of Asymmetric Vortical Flows over Delta Wings at High Angles of Attack," *J. Aircr.*, vol. 27, no. 5, pp. 429–435, 1990.

[28] D. Greenwell and N. Wood, "Roll Moment Characteristics of Asymmetric Tangential Leading-edge Blowing on a Delta Wing," *J. Aircr.*, vol. 31, no. 1, pp. 161–168, 1994.

[29] M. A. Ferman, L. J. Huttsell, and E. W. Turner, "Experiments with Tangential Blowing to Reduce Buffet Response on an F-15 Model," *J. Aircr.*, vol. 41, no. 4, pp. 903–910, Jul. 2004.

[30] N. Williams, Z. Wang, and I. Gursul, "Active Flow Control on a Nonslender Delta Wing," *J. Aircr.*, 2008.

[31] A. Kölzsch and C. Breitsamter, "Vortex-Flow Manipulation on a Generic Delta-Wing Configuration," *J. Aircr.*, vol. 51, no. 5, pp. 1380–1390, Apr. 2014.

[32] P. V Vorobieff and D. O. Rockwell, "Vortex Breakdown on Pitching Delta Wing: Control by Intermittent Trailing-edge Blowing," *Aiaa J.*, vol. 36, no. 4, pp. 585–589, 1998.

[33] M. Yavuz and D. Rockwell, "Control of Flow Structure on Delta Wing with Steady Trailing-Edge Blow," *AIAA J.*, vol. 44, no. 3, pp. 493–501, 2006.

[34] P. Jiang, Z. Wang, and I. Gursul, "Effects of Unsteady Trailing-Edge Blowing on Delta Wing Aerodynamics," *J. Aircr.*, vol. 47, no. 2, pp. 591–602, 2010.

[35] H. Johari, D. J. Olinger, and K. C. Fitzpatrick, "Delta wing vortex control via recessed angled spanwise blowing," *J. Aircr.*, vol. 32, no. 4, pp. 804–810, Jul. 1995.

[36] A. G. Sreenatha and T. K. Ong, "Wing Rock Suppression Using Recessed Angle Spanwise Blowing," *J. Aircr.*, vol. 39, no. 5, pp. 900–903, Sep. 2002.

[37] H. Johari and J. Moreira, "Delta wing vortex manipulation using pulsed and steady blowing during ramp-pitching," *J. Aircr.*, vol. 33, no. 2, pp. 304–310, Mar. 1996.

[38] N. J. WOOD, L. ROBERTS, and Z. CELIK, "Control of asymmetric vortical flows over delta wings at high anglesof attack," *J. Aircr.*, vol. 27, no. 5, pp. 429–435, May 1990.

[39] S. McCormick and I. Gursul, "Effect of Shear-layer Control on Leading-edge Vortices," *J. Aircr.*, vol. 33, no. 6, pp. 1087–1093, 1996.

[40] B. Badran and S. Mccormick, "Control of Leading-Edge Vortices with Suction," *J. Aircr.*, vol. 35, no. 1, pp. 163–165, 1997.

[41] A. M. Mitchell, D. Barberis, P. Molton, J. Dé, and lery, "Oscillation of Vortex Breakdown Location and Blowing Control of Time-Averaged Location," *AIAA J.*, vol. 38, no. 5, pp. 793–803, May 2000.

[42] C. Shih and Z. Ding, "Trailing-edge Jet Control of Leading-edge Vortices of a Delta Wing," *AIAA J.*, vol. 34, no. 7, pp. 1447–1457, 1996.

[43] Z. Wang, P. Jiang, and I. Gursul, "Effect of Thrust-Vectoring Jets on Delta Wing Aerodynamics," *J. Aircr.*, vol. 44, no. 6, pp. 1877–1888, 2007.

[44] M. Zharfa, "Control of Flow Structure on Low Swept Delta Wing With Steady Leading Edge Blowing," 2015.

[45] M. M. Yavuz and D. Rockwell, "Identification and Control of Three-Dimensional Separation on Low Swept Delta Wing," *AIAA J.*, vol. 44, no. 11, pp. 2805–2811, 2006.

[46] Y. Guy, J. Morrow, and T. McLaughlin, "Control of vortex breakdown on a delta wing by periodic blowing and suction," in *37th Aerospace Sciences Meeting and Exhibit*, American Institute of Aeronautics and Astronautics, 1999.

[47] and I. W. Y. Guy, J. Morrow, T. McLaughlin, "Pressure Measurements

and Flow Field Visualization on a Delta Wing with Periodic Blowing and Suction," in *AIAA Paper*, 1999.

[48] M. Gad-El-Hak and R. F. Blackwelder, "Control of the Discrete Vortices from a Delta Wing," *AIAA J.*, vol. 25, no. 8, pp. 1042–1049, 1987.

[49] S. Klute, R. Martin, O. Rediniotis, and D. Telionis, "Flow Control over Delta Wings at High Angles of Attack," *AIAA Pap.*, 1993.

[50] Q. Deng and I. Gursul, "Effect of leading-edge flaps on vortices and vortex breakdown," *Exp. Fluids*, vol. 23, no. 4, pp. 347–352, 1996.

[51] A. Mitchell and J. Délery, "Research into Vortex Breakdown Control," *Prog. Aerosp. Sci.*, 2001.

[52] E. Vardaki, I. Gursul, G. S. Taylor, and P. Student, "Physical Mechanisms of Lift Enhancement for Flexible Delta Wings," *AIAA Pap.*, no. January, pp. 1–13, 2005.

[53] T. Hu, Z. Wang, and I. Gursul, "Passive control of roll oscillations of low-aspect-ratio wings using bleed," *Exp. Fluids*, vol. 55, no. 6, 2014.

[54] T. I. National, E. A. Tics, R. Of, E. With, S. Wings, and B. G. Lachrnann, "No Title," 2017.

[55] M. Tanner, "Reduction of base drag," *Prog. Aerosp. Sci.*, vol. 16, no. 4, pp. 369–384, 1975.

[56] M. J. Hemscht and S. X. S. Bauer, "Alleviation of Side Force on Tangent-Ogive Forebodies Using Passive Porosity," *J. Aircr.*, vol. 31, no. 2, pp. 354–361, 1994.

[57] C. A. Hunter, S. A. Viken, and R. M. Wood, "Advanced Aerodynamic Design of Passive Porosity Control Effectors 39th AIAA Aerospace Sciences Meeting & Exhibit 8-11 January 2001 / Reno , NV," no. January 2001, 2017.

[58] P. W. Carpenter and L. J. Porter, "Effects of passive porous walls on boundary-layer instability," *AIAA J.*, vol. 39, no. 4, pp. 597–604, 2001.

[59] J. M. Kearney and A. Glezer, "Aerodynamic Control using Distributed Bleed," in *6th AIAA Flow Control Conference*, 2012, no. June, pp. 1–17.

[60] İ. Öztürk, "Experimental Analysis of Flow Structure on Moderate Sweep Delta Wing," vol. 25, no. 9, pp. 1682–1690, 2014.

[61] B. Yaniktepe and D. Rockwell, "Flow Structure on Diamond and Lambda Planforms: Trailing-Edge Region," *AIAA J.*, vol. 43, no. 7, pp. 1490–1500, Jul. 2005.

[62] M. M. Yavuz and D. Rockwell, "Control of Flow Structure on Delta Wing with Steady Trailing-Edge Blow," *AIAA J.*, vol. 44, no. 3, pp. 493–501, 2006.

[63] N. C. Lambourne and D. W. Bryer, "The bursting of leading-edge vortices - some observations and discussion of the phenomenon," *Aeronaut. Res. Counc.*, vol. 3282, pp. 1–35, 1961.

[64] D. Hummel, "Effects of Boundary Layer Formation on the Vortical Flow above Slender Delta Wings," no. October, pp. 4–7, 2004.

[65] F. M. Payne, T. T. Ng, R. C. Nelson, and L. B. Schiff, "Visualization and Wake Surveys of Vortical Flow over a Delta Wing," *AIAA J.*, vol. 26, no. 2, pp. 137–143, 1988.

[66] G. Taylor and I. Gursul, "Unsteady Vortex Flows and Buffeting of a Low Sweep Delta Wing," *42nd AIAA Aerosp. Sci. Meet. Exhib.*, no. January, pp. 1–9, 2004.

[67] R. Legendre, "Lignes de Courent d'un Ecoulement Continu," *Rech. Aerosp.h.*, vol. 105, pp. 3–9, 1965.

[68] A. E. Perry and H. Hornung, *Some aspects of three-dimensional separation. II - Vortex skeletons*, vol. 8. 1984.

[69] M. S. Chong and A. E. Perry, "Synthesis of Two- and Three-Dimensional Separation Bubbles," *9th Australian Fluid Mechanics Conference*. pp. 35–38, 1986.

[70] M. S. Perry, A. E. and Chong, "A DESCRIPTION OF EDDYING MOTIONS AND FLOW PATTERNS USING CRITICAL-POINT CONCEPTS," *Ann. Rev. Fluid Mech*, vol. 19, pp. 125–155, 1987.

[71] B. Dallman, U. and Schulte-Weming, "Topological Changes of Axisymmetric and Non-Axisymmetric Vortex Flows," in *Proceedings o f the IUTAM Symposium*, 1990, pp. 372–383.

[72] W. Su, M. Liu, and Z. Liu, *Topological Structures of Separated Flows About a Series of Sharp-Edged Delta Wings at Angles-of-Attack up to 90°", in Topological Fluid Mechanics (eds. H. K. Moffatt and A. Tsinober).* 1990.

[73] B. Lazos, "Surface Topology on the Wheels of a Generic Four-Wheel Landing Gear," *AIAA J.*, vol. 40, no. 12, pp. 2402–2411, 2002.

[74] S. J. Kline and F. A. McClintock, "Describing Uncertainties in Single-Sample Experiments," *Mech. Eng.*, p. p.3.

[75] A. Furman and C. Breitsamter, "Turbulent and unsteady flow characteristics of delta wing vortex systems," *Aerosp. Sci. Technol.*, vol. 24, no. 1, pp. 32–44, 2013.

[76] D. L. KOHLMAN and W. H. WENTZ, JR., "Vortex breakdown on slender sharp-edged wings," *J. Aircr.*, vol. 8, no. 3, pp. 156–161, 1971.

[77] M. V. Ol and M. Gharib, "Leading-Edge Vortex Structure of Nonslender Delta Wings at Low Reynolds Number," *AIAA J.*, vol. 41, no. 1, pp. 16–26, 2003.

[78] G. S. Taylor, T. Schnorbus, and I. Gursul, "An Investigation of Vortex Flows Over Low Sweep Delta Wings," *33rd AIAA Fluid Dyn. Conf. Exhib.*, no. June, pp. 1–13, 2003.

[79] O. Lucca-Negro and T. O'doherty, "Vortex breakdown: A review," *Prog. energy Combust. Sci.*, 2001.

[80] J. Lamar and J. F. Campbell, *Vortex flaps - Advanced control devices for supercruise fighters*, vol. 22. 1984.

[81] C. H. Kuo and N. Y. Lu, "Unsteady Vortex Structure over Delta-Wing Subject to Transient Along-Core Blowing," *AIAA J.*, vol. 36, no. 9, pp. 1658–1664, 1998.

[82] E. Vardaki, Z. Wang, and I. Gursul, "Flow Reattachment and Vortex Reformation on Oscillating Low-Aspect-Ratio Wings," *AIAA J.*, vol. 46, no. 6, pp. 1453–1462, 2008.

[83] Measurement Principles of PIV. (n.d.). Retrieved from https://www.dantecdynamics.com/measurement-principles-of-piv

[84] "INSIGHT 4G ™ GLOBAL IMAGE , ACQUISITION , ANALYSIS , & DISPLAY SOFTWARE," no. March, 2015.
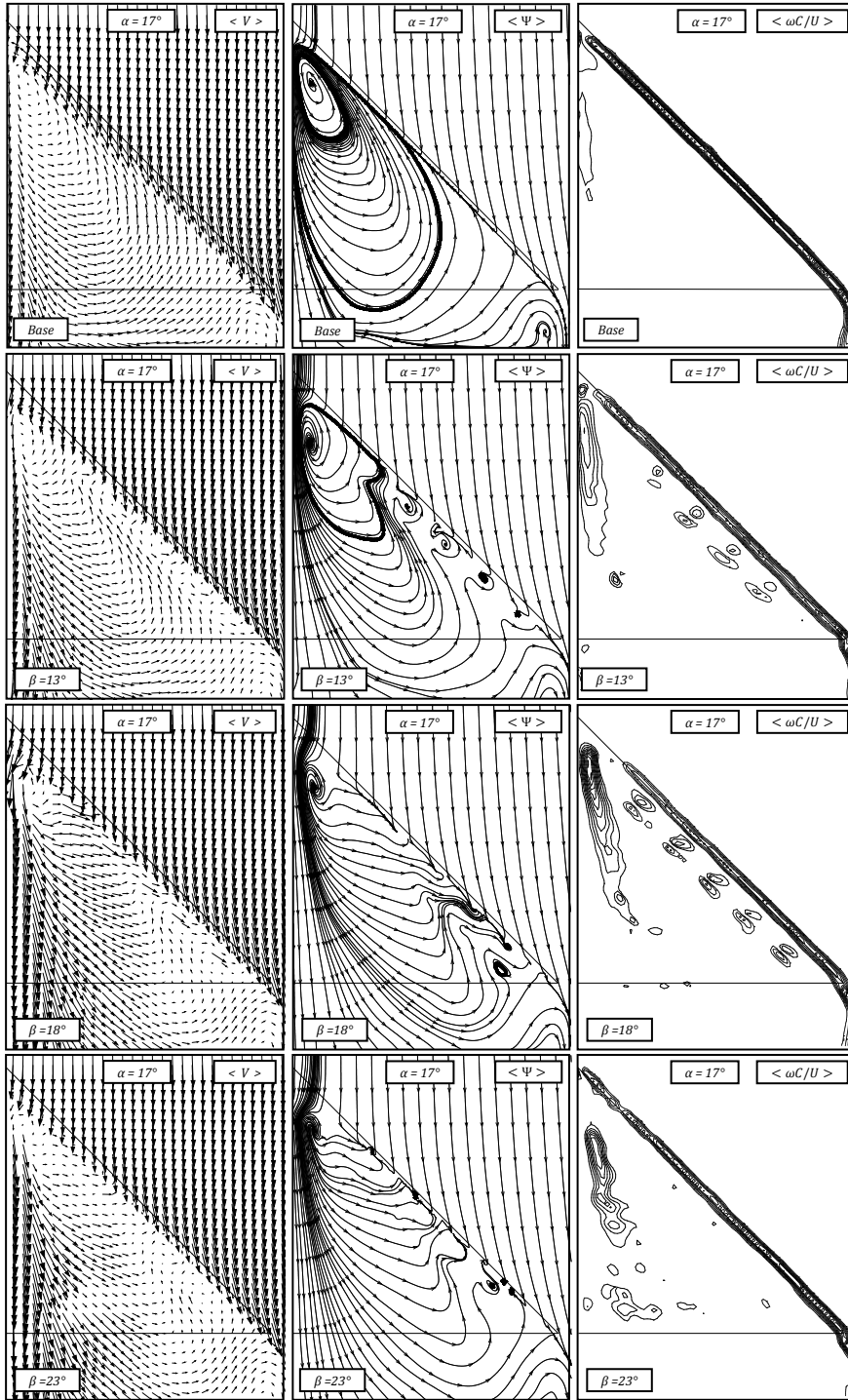
APPENDIX A

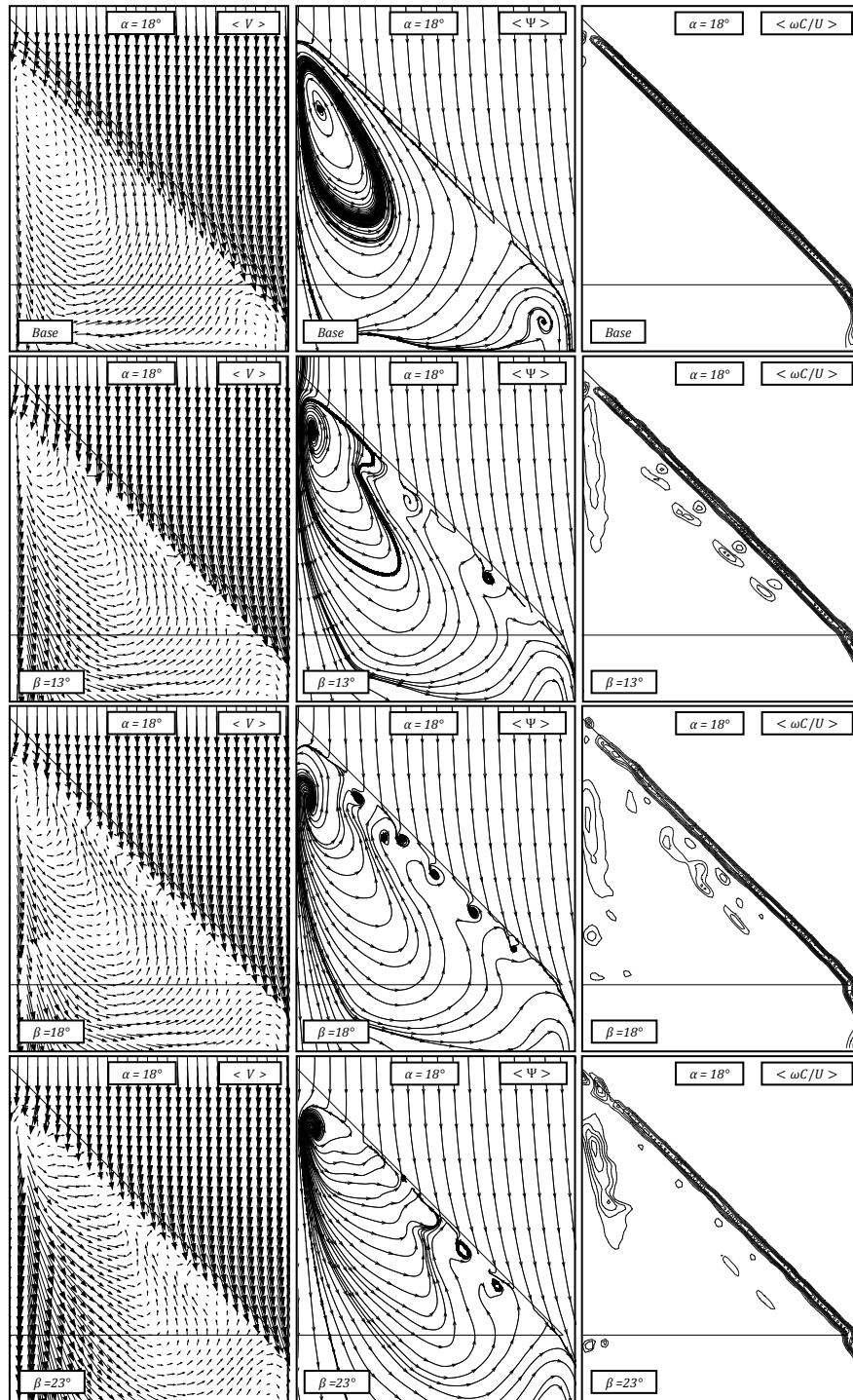## PIV RESULTS FOR BLEED EXPERIMENTS AT $\Delta z = 4$ mm
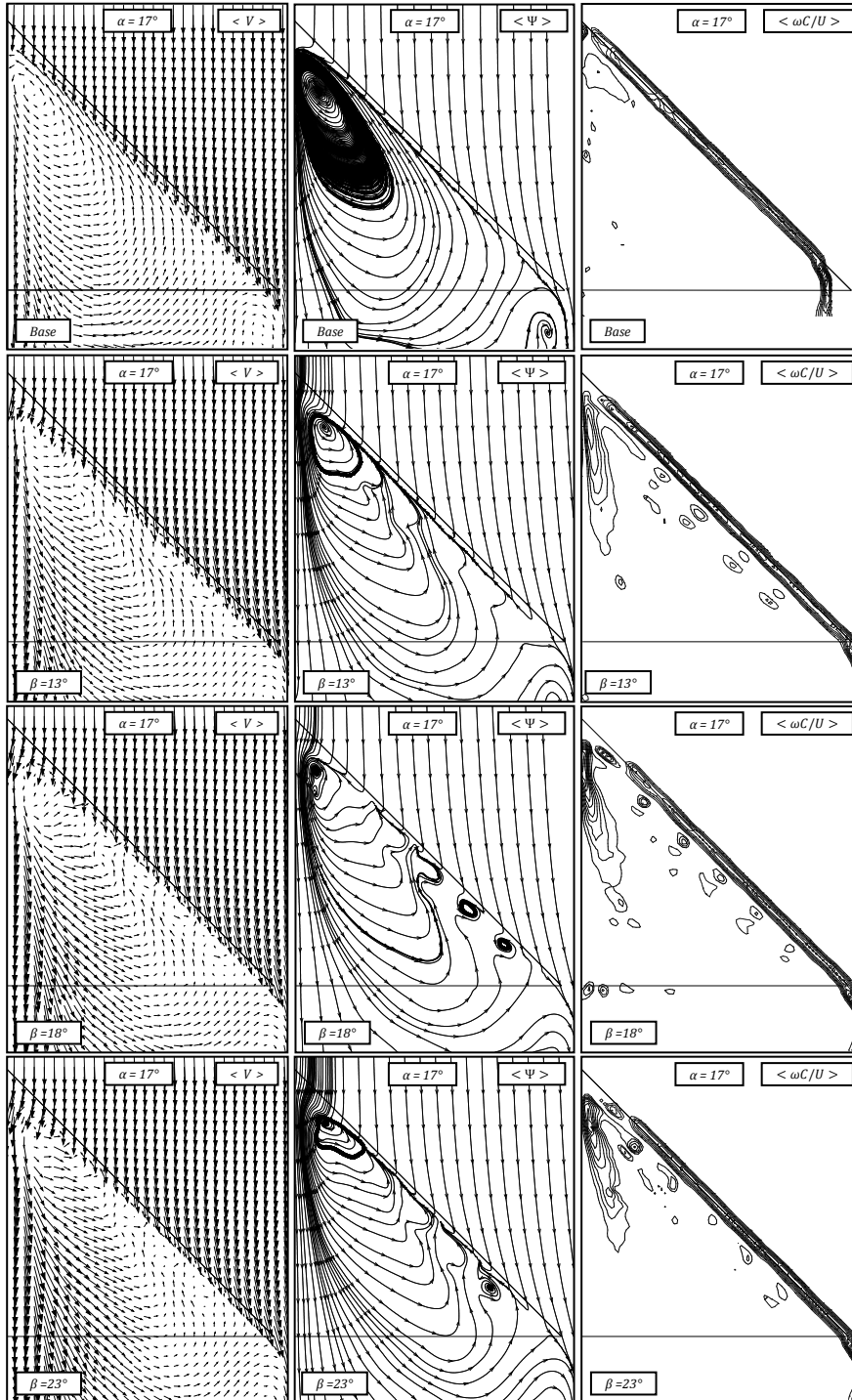
A 1 Patterns of time-averaged velocity vectors $\langle V \rangle$, streamlines $\langle \Psi \rangle$ and constant contours of non-dimensional vorticity $\langle \omega_z C/U \rangle$ at angle of attack $\alpha = 17$ deg for $Re = 3.5 \times 10^4$: $[|\langle \omega_z C/U \rangle|]_{min} = 54$, $\Delta[|\langle \omega_z C/U \rangle|] = 3$
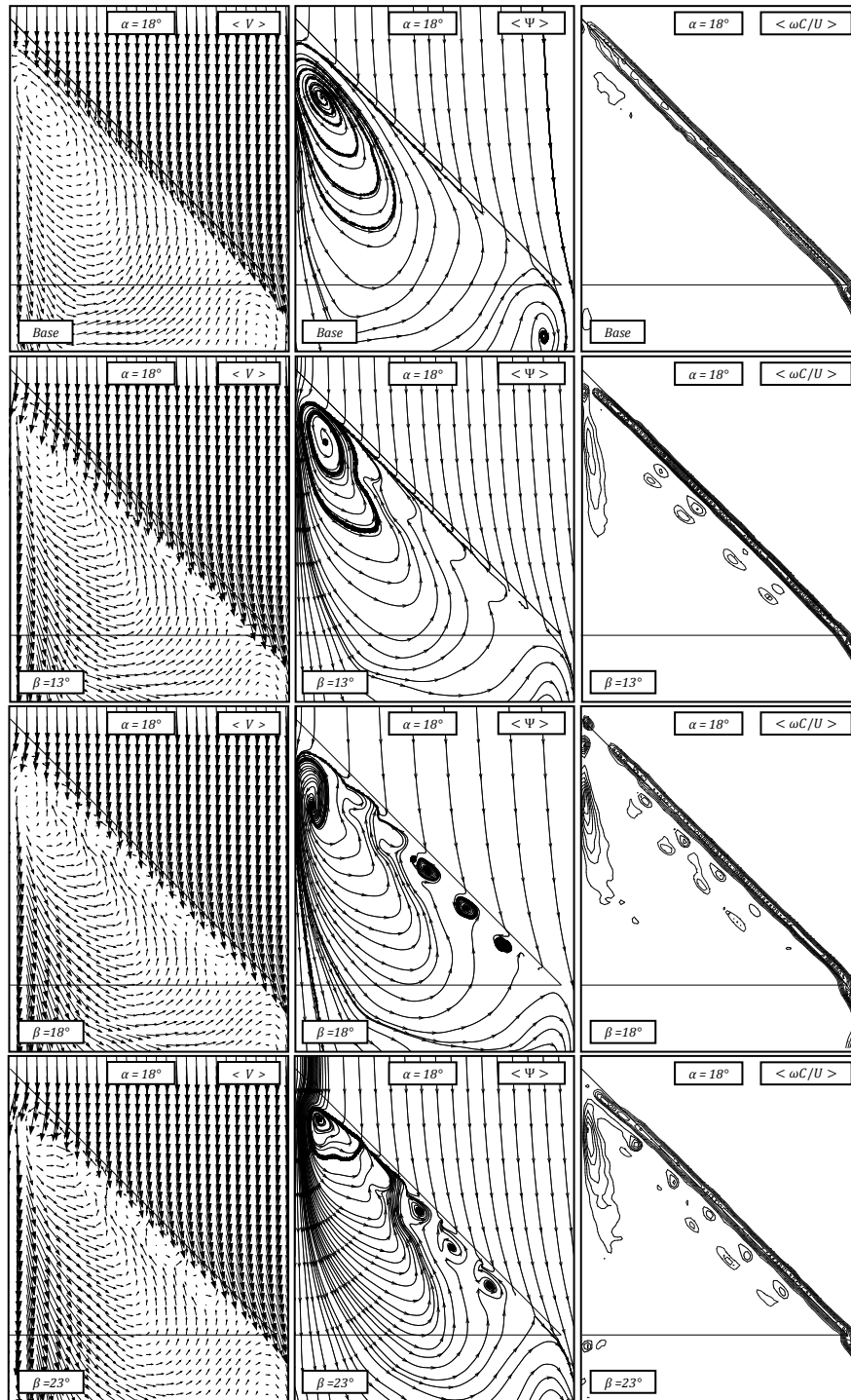
A 2 Patterns of time-averaged velocity vectors $\langle V \rangle$, streamlines $\langle \Psi \rangle$ and constant contours of non-dimensional vorticity $\langle \omega_z C/U \rangle$ at angle of attack $\alpha = 18$ deg for $Re = 3.5 \times 10^4$: $[|\langle \omega_z C/U \rangle|]_{min} = 54$, $\Delta[|\langle \omega_z C/U \rangle|] = 3$

A 3 Patterns of time-averaged velocity vectors $\langle V \rangle$, streamlines $\langle \Psi \rangle$ and constant contours of non-dimensional vorticity $\langle \omega_z C/U \rangle$ at angle of attack $\alpha = 17$ deg for $Re = 7.5 \times 10^4$: $[|\langle \omega_z C/U \rangle|]_{min} = 54$, $\Delta[|\langle \omega_z C/U \rangle|] = 3$
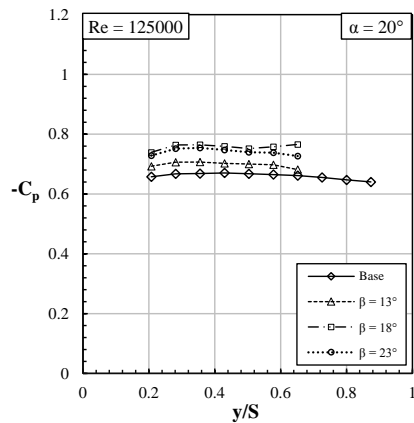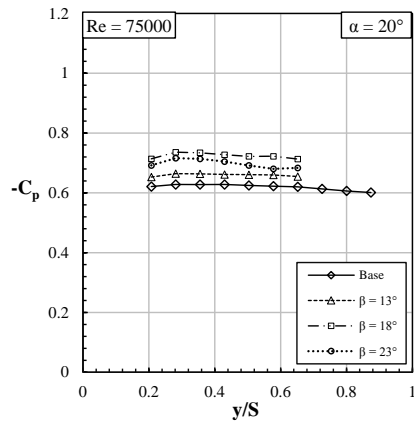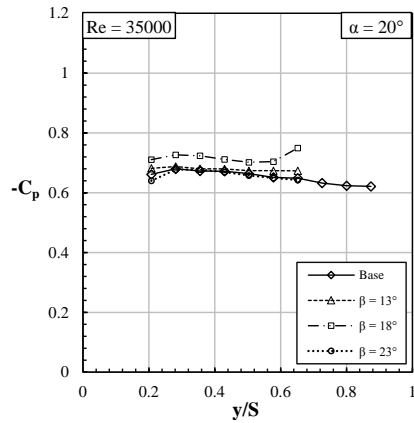
74

A 4 Patterns of time-averaged velocity vectors $\langle V \rangle$, streamlines $\langle \Psi \rangle$ and constant contours of non-dimensional vorticity $\langle \omega_z C/U \rangle$ at angle of attack $\alpha = 18$ deg for $Re = 7.5 \times 10^4$: $[|\langle \omega_z C/U \rangle|]_{min} = 54$, $\Delta[|\langle \omega_z C/U \rangle|] = 3$

75

APPENDIX B

PRESSURE MEASUREMENT RESULTS FOR BLEED EXPERIMENTS
AT $Re = 3.5 \times 10^4, 7.5 \times 10^4, 12.5 \times 10^4$ AND $\alpha = 20°$

B 1 $-C_p$ distributions of half span Base, $\beta = 13°$, $\beta = 18°$ and $\beta = 23°$ planforms at angle of attack $\alpha = 20$ deg at $Re = 3.5 \times 10^4, 7.5 \times 10^4, 12.5 \times 10^4$.

APPENDIX C

MATLAB CODE FOR PRESSURE MEASUREMENT UNCERTAINITY CALCULATIONS

```matlab
clear all
clc




%=======Uncertainty Calculation================
P_w=-25.95014621;        %%Pa (Static Pressure on the Wing)
P_inf=-17.42894893;      %%Pa (Static Pressure of the Free Stream)
P_stag=-9.155281591;     %%Pa (Stagnation Pressure of the Free
Stream
P_r=0.075;               %%Pa (Measurement Resolution of the Device
(0.003% FS))




Span=0.27;               %%m  (Wing Span, Measured with ruler)
Chord=0.135;             %%m  (Wing Chord, Measured with rules)
d_rul=0.001       %%m  (Resolution of ruler)
As=0.5*Span*Chord; %%m^2(Wing Surface Area)

%===========================================
%Uncertainty of Dynamic Pressure

P_dyn=P_stag-P_inf;
dPdyn_Pstag=1;
dPdyn_Pinf=-1;
dPdyn=((dPdyn_Pstag*P_r)^2+(dPdyn_Pinf*P_r)^2)^0.5

Urel_dPdyn=dPdyn/P_dyn    % (Relative uncertainty of Dynamic
Pressure)

%===========================================

%===========================================
%Uncertainty of Wing Surface Area
dAs_sp=0.5*Chord;
dAs_ch=0.5*Span;
dAs=((dAs_sp*d_rul)^2+(dAs_ch*d_rul)^2)^0.5;

Urel_dAs=dAs/As    % (Relative uncertainty of Wing Surface Area)

%===========================================
%Uncertainty of Pressure Coefficient

Cp=(P_w-P_inf)/(P_stag-P_inf);
```

77

```matlab
dCp_Pw=1/(P_stag-P_inf);
dCp_Pinf=(P_w-P_stag)/(P_inf-P_stag)^2;
dCp_Pstag=(P_inf-P_w)/(P_inf-P_stag)^2;

dCp=((dCp_Pw*P_r)^2+(dCp_Pinf*P_r)^2+(dCp_Pstag*P_r)^2)^0.5

Urel_Cp=dCp/-Cp % (Relative uncertainty of Pressure Coefficient)

%============================================
```